Computation of rotor wake turbulence noise

M. Nallasamy[a,*], E. Envia[b]

[a]QSS Group, Inc., NASA Glenn Research Center, Cleveland, OH 44135, USA
[b]Acoustics Branch, NASA Glenn Research Center, Cleveland, OH 44135, USA

Abstract

A major source of fan broadband noise is the interaction of rotor wake turbulence with the fan outlet guide vanes. A broadband noise model that utilizes computed rotor flow turbulence from a Reynolds averaged Navier–Stokes code is used to predict fan broadband noise spectra. The noise model is employed to examine the broadband noise characteristics of the 22-in source diagnostic test fan rig for which broadband noise data were obtained in wind tunnel tests at the NASA Glenn Research Center. A 9-case matrix of three outlet guide vane configurations at three representative fan tip speeds are considered. For all cases inlet and exhaust spectra of acoustic power are computed and compared with the measured spectra where possible. The acoustic power levels and shape of the predicted spectra are in good agreement with the measured data for the fan exhaust duct radiation at approach condition where direct comparisons are possible. The predicted spectra show the experimentally observed trends with fan tip speed, vane count and vane sweep. The results also demonstrate the validity of using computational fluid dynamics based turbulence information for fan broadband noise calculations.
© 2004 Elsevier Ltd. All rights reserved.

1. Introduction

Owing to the success of fan tone noise reduction techniques [1], fan broadband noise is now widely acknowledged as the next major obstacle to be overcome in attempts to reduce aircraft engine noise. But, unlike tone noise the sources of fan broadband noise are many and most are not

*Corresponding author.
  E-mail address: nallasamy@grc.nasa.gov (M. Nallasamy).

as well understood. In response to this challenge a number of theories [2–5] have been devised to help elucidate the nature and characteristics of fan broadband noise. These theories require flow turbulence characteristics (i.e., spectrum, intensity, length scales, etc.) as input for computing noise spectra. Typically, such information is available from experiments [6,7] or is simply guessed at to provide the best fit of the predicted noise spectra to the measured ones. An alternative approach is to compute the turbulence characteristics using a Reynolds averaged Navier–Stokes (RANS) type calculation, since that would provide a true prediction capability.

This paper presents one such attempt that combines predicted flow turbulence characteristics obtained from a turbomachinery computational fluid dynamics (CFD) code with a fan broadband noise theory to compute fan noise spectra. The flow code called APNASA [8], is a three-dimensional Navier–Stokes solver with an improved k–ε turbulence model [9]. The fan broadband noise code is a revised and enhanced version of an analytical noise prediction theory originally developed by Ventres et al. [10]. The testbed is a $\frac{1}{5}$-scale model of a representative high bypass ratio turbofan engine for which extensive aerodynamic and acoustic data were obtained [11–13]. Only the broadband noise produced by the interaction of fan wake turbulence with the stator outlet guide vanes (OGV) will be considered here. The data theory comparisons will be done on an acoustic power basis since the noise theory furnishes acoustic power predictions only.

The 22-in diameter model fan was tested in the NASA Glenn Research Center's $9' \times 15'$ acoustic wind tunnel. The fan has 22 blades and a design tip speed of 1215 ft/s. The baseline OGV has 54 radial vanes and represents a conventional "cut-off" stator design (i.e., the blade passing frequency is cut-off). The low-count OGV is a "cut-on" concept, which has only 26 radial vanes but has the same solidity as the baseline stator. The smaller vane count was selected to reduce broadband noise [14]. The swept OGV has 26 swept vanes (with 30° sweep) and was designed to minimize the blade passing frequency tone penalty associated with a cut-on design. The sketches of the fan stages along with the photographs of the partially assembled fan stages are shown in Fig. 1.

The aerodynamic and acoustic tests were conducted over a wide range of fan operating conditions for each of the three OGV packs. For the purposes of the current work, however, only the speeds corresponding to the noise certification points (approach, cutback, and takeoff) will be discussed. The relevant fan operating conditions are listed in Table 1.

In what follows, a summary of the analysis tools used in this work will be presented followed by a discussion on theoretical results and their comparison with measured data (where possible). The paper concludes with a summary of important results.

2. Analysis

The input for the noise prediction was generated by means of a series of CFD simulations of the fan rotor coupled with the fan outlet guide vane. The code used to generate the fan flow field is APNASA (see Ref. [8]), which solves for the time-average flow field in a typical passage of a blade row embedded within a multistage turbomachine. The simulations are three-dimensional and include the effect of viscosity. A modified k–ε turbulence model (see Ref. [9]) was used to account for the effect of turbulence mixing.
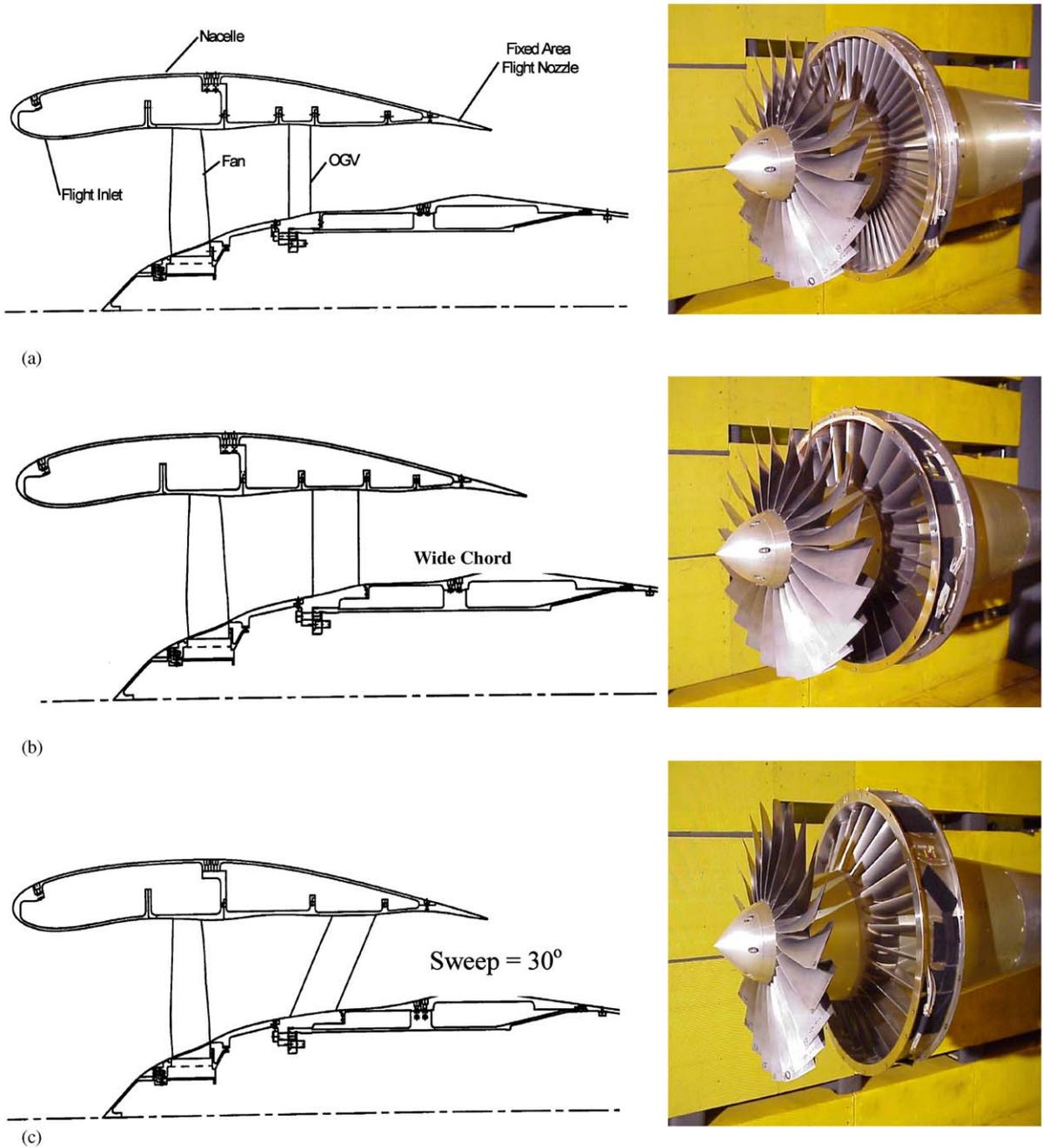
Fig. 1. Photographs of partially assembled fan stages and corresponding sketches: (a) baseline: 54 radial vanes, (b) low count: 26 radial vanes, (c) low noise: 26 swept vanes.

Table 1
Fan operating conditions of interest

Power setting	Corrected fan rpm (rev/min)	Corrected fan tip speed (fps)
Approach	7808	750
Cutback	11,074	1060
Takeoff	12,656	1215

To do the CFD simulation, first it is necessary to establish the fan rotor geometry at test conditions, since fan rotors untwist as they are run-up in rotational speed. It is well known that the effect of rotation on fan rotor shape has significant impact on aerodynamic performance. In addition, the operating conditions considered here (see Table 1) include both design and off-design conditions, involving a wide range in fan rotational speed. Hence, at each rotational speed in Table 1, the fan rotor blade running (or hot) shape is established using a coupled aero/structural analysis system [15].

The system starts with the manufactured blade shape (or the cold shape) and a specified fan rotor rpm, and iterates between the structural and aerodynamic sections of the coupled system. Output from the structural analysis is post-processed to generate a flow field grid for the CFD simulation. The output of the CFD simulation is post-processed to find the aerodynamic load on the rotor blade. This information is supplied to the structural analysis system to update the structural analysis inputs. This cycle is repeated until convergence (i.e., no significant change in fan rotor geometry) is obtained. Upon convergence, the fan rotor blade running (hot) shape is established along with its flow field. The rotor blade shape thus obtained accounts for both centrifugal loading and aerodynamic loading on the blade.

2.1. Rotor wake flow field

A typical example of the CFD results of the rotor flow field for the baseline, 54 radial vane fan stage configuration compared to the laser Doppler velocimetry (LDV) data at the takeoff condition (where direct one to one comparison is possible (see Refs. [6,7])) is presented in Fig. 2. (This solution was obtained with a CFD grid having 407 grid cells in the axial direction, 51 grid cells in the radial direction and 51 grid cells in the azimuthal direction.) The plots show the comparisons for an axial location 2 in downstream of the rotor trailing edge (at the tip). The time-averaged axial velocity contours are shown in these figures. The contours depict average passage results, with the average passage data duplicated circumferentially to provide a better view of the flow. (In this view, the rotor blades rotate clockwise.) The rotor wake structure obtained from the CFD solution is in excellent agreement with the LDV data. Note that the agreement extends over the entire span including the hub and tip regions.

The turbulence intensity and length scales derived from the CFD simulations at the stator leading edge were used to prescribe the wake turbulence field impinging on the outlet guide vane. This information and the time average flow field of the outlet guide vane formed the input to the acoustic predictions. It should be noted that the input was used "as is" and no adjustments were made to the input to achieve a better agreement with data.
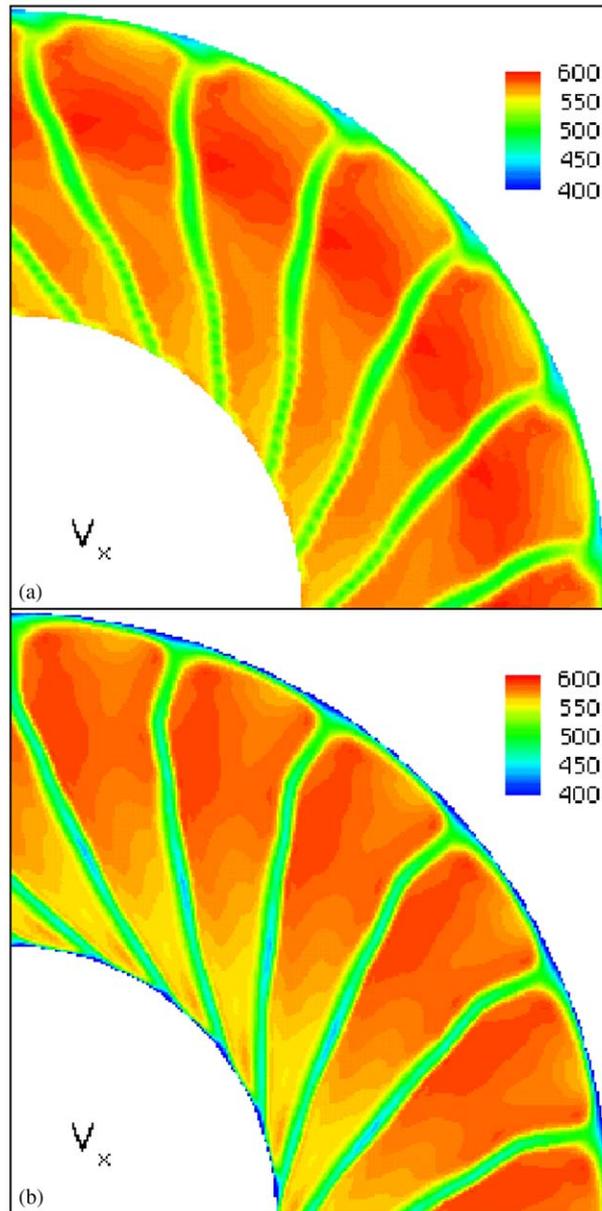
Fig. 2. Comparison of (a) experimental and (b) CFD results for the baseline configuration at takeoff at 2 in behind the rotor: *axial velocity*.

2.2. Rotor wake turbulence noise model

The rotor–stator broadband noise prediction model used for this study is based on a theory developed by Ventres et al. [10]. However, significant enhancements were made to the original theory and a new code was written to take full advantage of the flow turbulence information

available from the RANS solutions. The salient features of the modified model are briefly described below.

Predicated on a modal description of the noise field inside the fan duct, the theoretical model ultimately relates the spectral density of the duct modes to the spectral density of the incident turbulence. As an intermediate step, the unsteady pressure distribution on the stator is tied to the incident turbulence at each frequency $\omega = 2\pi f$. This is done on a strip-wise basis assuming that turbulence is locally isotropic at each radius with its statistics parametrically dependent on the radius. The resulting distribution of stator unsteady pressure is then related to the duct mode amplitude via the Green's function formulation [10]. The end results can be written (in short-hand notation) as

$$\langle |p_{mn}(\omega)|^2 \rangle = \int_{r_H}^{r_T} |C_{mn}(r,\omega)|^2 \psi_m^2(\kappa_{mn}r)\Phi(r,\omega)\,\mathrm{d}r, \tag{1}$$

where $\langle |p_{mn}(\omega)|^2 \rangle$ is the spectral density of duct mode pressure, C_{mn} is the chordwise integral of the stator unsteady pressure at each radius, and ψ_m is the annular duct mode shape. r_H is the hub radius and r_T is the tip radius. The chordwise integral C_{mn} is expressed as

$$C_{mn}(r,\omega) = \frac{1}{b}\int_{-b}^{b} f(r,z,k,\omega)\mathrm{e}^{\mathrm{i}\mu z}\,\mathrm{d}z,$$

where $\mu = \gamma_{mn}\cos(\alpha) - (m/r)\sin(\alpha)$, γ_{mn} the wavenumber in the x direction of the mn mode, m representing the circumferential order and n the radial order, α the vane stagger angle, z the chordwise variable, ω the radian frequency, k the wavenumber vector, and b the vane semi-chord.

The elemental loading function, f, depends only parametrically on the radius, r, and is the same on each vane. In other words, a spanwise array of 2-D unsteady pressure fields is coupled to a 3-D duct acoustic field.

The annular duct normal mode shape function is given by

$$\psi_m(\kappa_{mn}r) = [AJ_m(\kappa_{mn}r) + BY_m(\kappa_{mn}r)],$$

where κ_{mn} is the eigenvalues of annular duct modes, J_m, Y_m are the Bessel functions of the first and second kind, respectively, and A and B are constants.

The function Φ represents the spectral density function of the incident turbulence given by

$$\Phi(r,\omega) = N_V^2 L_r \left\{ \frac{(N_B L_w u_w')^2}{(2\pi)^2 \bar{r}^3} \sum_{m_1=-\infty}^{\infty} \sum_{q_1=-\infty}^{\infty} \left(\mathrm{e}^{-\frac{1}{4\pi}\left(\frac{m_1 N_B L_w}{\bar{r}}\right)^2} \right)^2 L_1 L_2 \tilde{\phi}_1\left(\lambda_1^{(w)}L_1\right)\tilde{\phi}_2\left(\lambda_2^{(w)}L_2\right) \right.$$

$$+ \frac{N_B L_w u_b' u_w'}{2\pi \bar{r}^2} \sum_{q_1=-\infty}^{\infty} \mathrm{e}^{-\frac{1}{4\pi}\left(\frac{m_1 N_B L_w}{\bar{r}}\right)^2} \left[L_1 L_2 \tilde{\phi}_1\left(\lambda_1^{(w)}L_1\right)\tilde{\phi}_2\left(\lambda_2^{(w)}L_2\right) + L_1 L_2 \tilde{\phi}_1\left(\lambda_1^{(b)}L_1\right)\tilde{\phi}_2\left(\lambda_2^{(b)}L_2\right) \right]$$

$$\left. + \frac{u_b'^2}{\bar{r}} \sum_{q_1=-\infty}^{\infty} L_1 L_2 \tilde{\phi}_1\left(\lambda_1^{(b)}L_1\right)\tilde{\phi}_2\left(\lambda_2^{(b)}L_2\right) \right\}. \tag{2}$$

In this expression, it is assumed that the auto-correlation function of the rotor wake turbulence is approximated as a product of three functions each which depends only on one variable. This is done to enable the use of experimental or computed (as in the present paper) data to select an appropriate correlation function. The correlation function assumed is with the corresponding

integral length scales in the three principal directions,

$$\phi(\underline{x}, \Delta r) = \phi_1(x_1/L_1)\phi_2(x_2/L_2)\phi_r(\Delta r/L_r).$$

Further, it is assumed that the radial integral scales are small, and the integral over Δr is approximated by the infinite integral

$$\int \phi_r(\Delta r/L_r)\,\mathrm{d}(\Delta r) = L_r.$$

This is further discussed below and in Appendix A where a complete derivation of the noise model is given.

In deriving Eq. (2), it is assumed that the rms turbulence intensity distribution consists of two parts. One is a constant background turbulence level representing the circumferentially averaged intensity of turbulence that is ingested by the fan. The other is a Gaussian distribution representing the turbulence intensity variations within the individual rotor blade wakes. The sum of the two contributions denotes the rms rotor turbulence level u' given by

$$u'(r) = u'_b(r) + u'_w(r)\mathrm{e}^{-\xi^2/L_w^2}, \tag{3}$$

where ξ is along the pitchwise direction measured normal wake centerline and L_w denotes the width of the Gaussian profile which is a function of radius. In this equation u'_b denotes the background rms turbulence intensity and u'_w denotes the wake centerline rms turbulence intensity.

In developing the original theory only an equivalent Gaussian profile contribution was taken into account. This leads to excessively large spectral fall-off rates since the Gaussian tends to zero away from the wake centerline instead of to the non-zero background intensity levels observed behind the rotor.

As a result of the modified representation for intensity distribution, the new noise model now includes three terms in Eq. (2) instead of a single term as in the original formulation of the theory. In the new model, the background turbulence contribution (i.e., the term containing u'^2_b) sets the spectrally broad background levels while the wake turbulence contribution (i.e., the term containing u'^2_w) contributes to the spectrum in the vicinity of the blade passing frequency harmonics. The mixed term (i.e., the term containing $u'_b u'_w$) provides the blending between the two.

In Eq. (2), $\tilde{\phi}_1$ and $\tilde{\phi}_2$ denote cross spectral densities of turbulence in the axial and tangential directions with L_1 and L_2 the corresponding integral length scales. It has been assumed that the integral length scale in the radial direction (i.e., L_r) is small compared with the stator span and that the overall cross-spectral density function is a product of cross-spectral density functions in the axial and tangential directions. N_B and N_V denote the blade and vane counts.

It should be pointed out that Eq. (1) was derived by assuming that the stator is an ensemble of zero thickness flat plates in an infinite hard-wall annular duct containing a uniform axial mean flow (see Appendix A). The parameters controlling the unsteady pressure distribution on the stator are the absolute Mach number of the mean flow and stator vane chord, vane count and stagger angle at each radius (i.e., strip). In particular, in this work, the vane cascade stagger angle is defined as a weighted average of the airfoil section camber line angles at the leading and trailing edges. The leading edge contribution is weighted more (90%) as compared to the trailing edge contribution (10%) in recognition of the fact that the high-frequency unsteady pressure distribution on the vane is concentrated near its leading edge.

As was mentioned earlier, the turbulence input information for this work was obtained from CFD simulations. The necessary input for the noise model includes the background and wake centerline turbulence intensities (u'_b and u'_w) as well as the turbulence integral length scales (L_1, L_2 and L_r). The intensities were obtained by extracting the intensity distribution from the RANS solution via

$$u'_{\text{RANS}} = \sqrt{\tfrac{2}{3}k_{\text{RANS}}}, \tag{4}$$

where k_{RANS} is the computed local kinetic energy of turbulence. The form of Eq. (4) is a reflection of the fact that the turbulence model used in the RANS calculations is isotropic. As shown in Fig. 3, a fit of the form given by Eq. (3) is in good agreement with the pitchwise distribution of u'_{RANS}. Note that the computed u'_{RANS} from k–ε model is set equal to wake turbulence u'_w and the background turbulence u'_b is also extracted from the same solution. The fitted distribution is assumed to apply to all rotor blade passages so that the pattern repeats around the annulus. Note that this does not mean that the instantaneous turbulent fluctuations are the same for corresponding points in passages, but only their statistics. The same argument applies to the length scales also which are estimated from the computed RANS flow field solutions via

$$L_{\text{RANS}} = c\bar{k}_{\text{RANS}}^{3/2}/\bar{\varepsilon}_{\text{RANS}}, \tag{5}$$

where $\bar{k}_{\text{RANS}}$ and $\bar{\varepsilon}_{\text{RANS}}$ are the circumferentially averaged turbulence kinetic energy and dissipation computed from the RANS solution. Defined in this manner, L_{RANS} is the average size of the largest energy containing eddy in the flow and the computed length (with the constant c set to unity) compared well with the measured integral length scale.
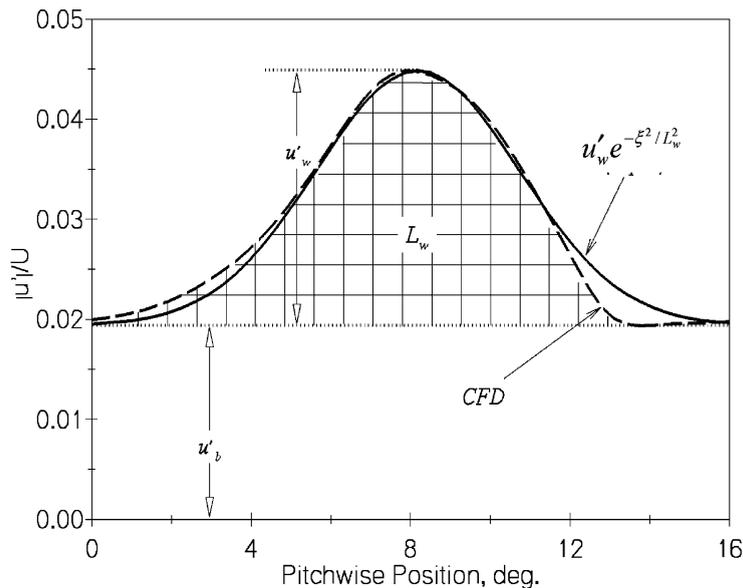

Fig. 3. A representative turbulence intensity profile: dashed line denotes the CFD solution and the solid line the fit using Eq. (3).

Three integral length scales are needed for the computation as indicated above. But we have only one length scale computed from the current RANS calculations since the solution procedure employs a k–ε turbulence model. We associate this computed length scale L_{RANS} with the longitudinal integral length scale. From the experiments on the fan rotor wake flow at low Mach numbers such as considered here, it is found that the tangential length scale is nearly equal to the longitudinal length scale, and we set L_1 equal to L_2.

We assume that the wake turbulence is isotropic. Then, the transverse length scale is equal to one-half of the longitudinal length scale. Thus, in the computations presented in this paper we have set

$$L_1 = L_{\mathrm{RANS}}, \quad L_2 = L_{\mathrm{RANS}}, \quad L_r = L_{\mathrm{RANS}}/2. \tag{6}$$

Once the power spectrum for each duct mode is computed using Eq. (1), the expected value of the acoustic power flux within the duct for that mode is computed as indicated below.

In a uniform duct flow with axial velocity U, the acoustic intensity is given by

$$I = (1 + M^2)pu + \frac{M}{\rho_o c_o} p^2 + \rho_o c_o M u^2, \tag{7}$$

where $M = U/c_o$ is the nominal axial flow Mach number, ρ_o is the nominal fluid density and p, ρ, and u are the instantaneous acoustic perturbation pressure, density, and axial velocity, respectively. The instantaneous sound power is found by integrating the intensity over the cross section of the duct.

The resulting expression for the power flux per mode, $S_{mn}(\omega)$, is written as

$$S_{mn}(\omega) = \frac{\pi(r_t^2 - r_H^2)}{\rho_o U} \left\{ \frac{\mp M^2(1 - M^2)^2(\omega/U)k_{mn}(\omega)}{[\omega/c_o \pm Mk_{mn}(\omega)]^2} \right\} p_{mn}(\omega), \tag{8}$$

where $k_{mn} = \{(\omega/c_o)^2 - (1 - M)^2 \kappa_{mn}^2\}^{1/2}$ and the upper set of signs refer to energy flow upstream of the stator (in the negative x-direction) and the lower set refers to the downstream propagation. Then, the total sound flux is obtained by summing over all the modes m and n,

$$S(\omega) = \sum_m \sum_n S_{mn}(\omega). \tag{9}$$

The variations (as a functions of radius) of the local Mach number, vane stagger angle, incident turbulence intensity and integral length scales, and the effective width of the intensity profiles are inputs for noise spectra computations. For each case considered in this work, this information was extracted from the corresponding CFD solution. Thus, the three dimensional (3-D) acoustic response of an annular cascade with a uniform flow for a prescribed incident rotor wake turbulence is computed. Both upstream radiated (inlet) and downstream radiated (exhaust) noise are computed in terms of acoustic power for each cut-on circumferential mode order, m and radial mode order, n at each radial strip. The noise is summed over all the radial strips along the vane span to obtain radiated acoustic power at each frequency.

2.3. Measured noise spectra for comparisons

The acoustic measurements were made in the NASA Glenn $9' \times 15'$ acoustic wind tunnel. Fig. 4(a) shows the photograph of the model fan installed in the tunnel. Sideline acoustic data were acquired with a computer controlled translating microphone probe indicated on the photograph and also on the sketch (Fig. 4(b)). The translating microphone probe acquired data at 48 sideline geometric angles from $27.2°$ to $134.6°$ relative to the fan rotor plane. The translating probe was at a distance of $89''$ (about four fan diameters) from the fan rotational axis. Also, there were three aft microphones fixed to the tunnel floor (see Fig. 4(b)) to acquire acoustic data at geometric angles of $140°$, $150°$, and $160°$. Data were also acquired with an acoustic barrier wall installed adjacent to the fan (Fig. 4(c)) which effectively blocked noise radiated through the fan aft duct, thus measuring only the fan inlet radiated noise. The fan exhaust noise is then obtained, subtracting the fan inlet noise (Fig. 4(c)) from the total noise measured without an acoustic barrier (Fig. 4(b)).

To be able to separate the rotor–stator interaction noise from the total fan stage noise, data were acquired for two configurations namely (1) the rotor + stator configuration of a regular fan stage (Fig. 5(a)) and (2) the rotor alone configuration (Fig. 5(b)). For each of these configurations data were acquired with and without the acoustic barrier wall (Fig. 4) as described above. Thus, it is possible to separate the rotor–stator interaction noise alone, knowing the rotor alone noise. And then, from the acoustic barrier wall measurements, the interaction noise radiated through the fan inlet duct and that radiated through the fan exhaust duct are separated. The process of noise separation in this manner is described below with examples of measured acoustic spectra.

Fig. 6(a) shows the measured spectrum of total (inlet plus exhaust) acoustic power for rotor–stator combination from which the rotor-alone contribution is subtracted to get the OGV power level. Fig. 6(b) shows the use of the measurements with the barrier wall (which blocks the exhaust radiation reaching the inlet). Here again, rotor–stator combination and rotor-alone spectra are available. This enables the separation of the OGV inlet noise spectrum. Subtracting the inlet contribution from the inlet plus exhaust spectrum for OGV in Fig. 6(a), the exhaust spectrum of OGV alone is obtained (see Fig. 6(c)). In practice, however, that proved problematic for all but the approach condition, since at high fan tip speeds, the rotor-alone levels tend to be higher than the stage (i.e., rotor plus stator) levels. Furthermore, since the current noise model does not account for the swirl flow between the rotor and stator or the transmission loss effects through the rotor, *inlet* noise predictions do not fully reflect the correct physics and as such are not expected to result in good comparisons with the data.

Therefore, the data-theory comparisons for the fan inlet and the exhaust noise are made at the approach speed only. However, predicted *trends* with the fan tip speed on the fan exhaust radiated noise are presented and compared with the data. The effect vane count and vane sweep on acoustic power are presented for the exhaust radiation at approach condition only and compared with the measured spectra.

3. Results and discussion

For all nine cases the inlet and exhaust duct acoustic power levels were computed for frequencies up to $50\,\text{kHz}$. This range corresponds approximately from 0.5BPF (blade passing

Fig. 4. Noise source separation: inlet/exhaust noise separation: (a) photograph of the source diagnostic test model installed in the NASA Glenn 9×15 ft wind tunnel, (b) sketch showing the no-barrier measurement setup, (c) sketch showing measurement setup with acoustic barrier.
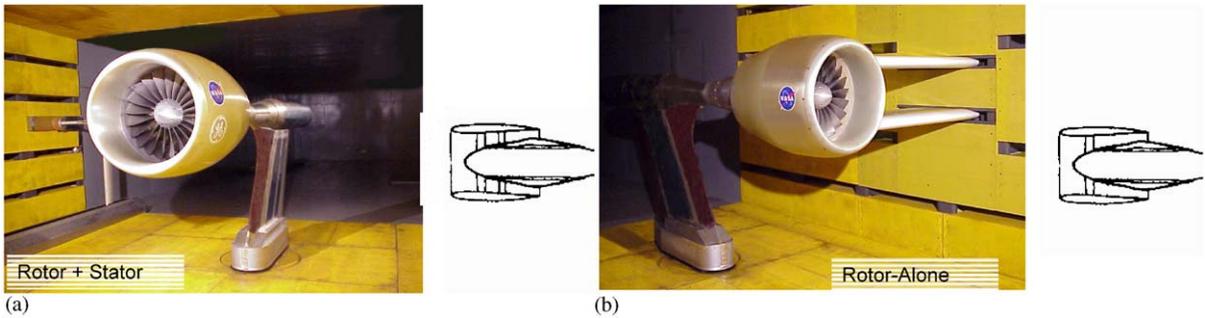
Fig. 5. Noise source separation: rotor/stator noise separation: (a) rotor plus stator (noise) configuration, (b) rotor alone (noise) configuration.
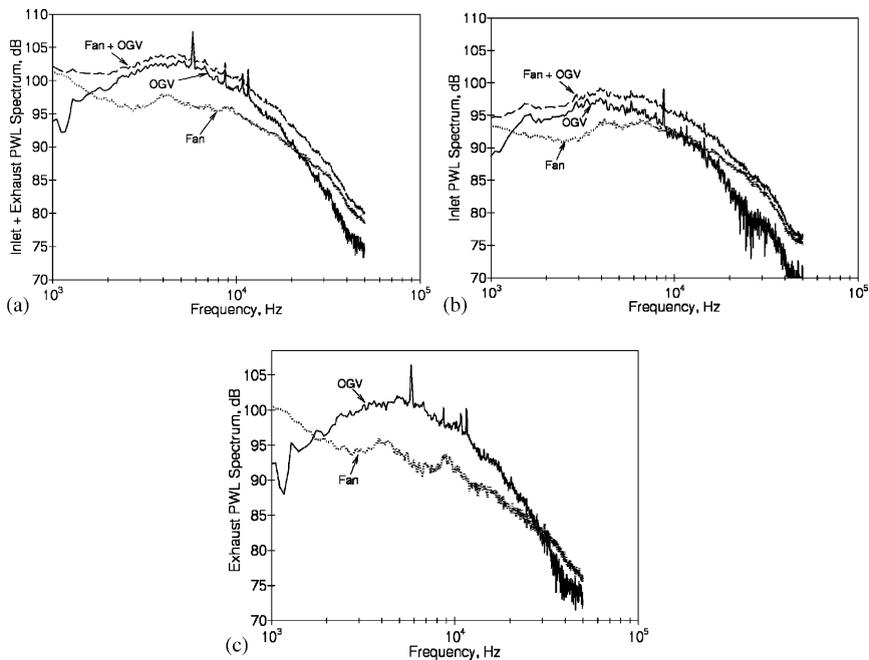

Fig. 6. Separation of measured inlet noise from exhaust noise and rotor noise from stator (OGV) noise. Frames (a) through (c) show various stages of separation. Baseline stator: approach.

frequency) to 11BPF for takeoff, 0.5BPF to 13BPF for cutback, and 0.5BPF to 18BPF for approach.

The spectral calculations were typically done at 0.5BPF increments, since the number of cut-on modes that must be computed increases (see Section 3.5) so rapidly that smaller frequency increments would have significantly increased the computational time. In the following figures for data theory comparisons, the symbols denote the frequency points at which the spectral calculations were actually performed and the lines through the symbols are curve fits to provide an idea of the spectral shapes.

It should be pointed out that, occasionally, the computed amplitude of the aerodynamic response of one of the strips would be inordinately large due to local cascade resonance condition. This, in turn, would lead to a "wild" point in the associated acoustic response. By slightly adjusting the aerodynamic input parameters, the resonance point could be avoided. However, in this paper the occasional wild point has been eliminated from the computed spectra. In a 3-D response, such local resonance conditions would not occur.

3.1. Comparisons with the measured spectra

First, the data-theory comparison is presented in terms of the spectra of acoustic power at the approach operating condition for all the stator configurations. Figs. 7–9 show the predicted and measured spectra for the baseline 54 radial vanes, 26 radial vanes, and 26 swept vanes configuration, respectively. In each case, the left figure shows the inlet noise spectra and the right figure shows the exhaust noise spectra. Note that the measured spectra contain BPF tone harmonics. While the BPF tone is cut-off (and absent) for the baseline case, it is cut-on (and present) for the other two cases. The current predictions have only the broadband noise component.

The predicted shape of the exhaust noise spectra in all three cases is in fairly good agreement with the measured spectra including the high-frequency fall off (Figs. 7(b), 8(b), and 9(b)). However, there is an under-prediction of levels which may arise from several factors. The main one is the fact that the measurements may have contributions from additional noise sources while the predictions account for only the rotor wake turbulence. Also, at high frequencies quadrupole noise may contribute to the power levels, as discussed by Mani et al. [16], and may have to be included in the prediction procedure to enhance the comparisons.

The computed inlet noise spectra (Figs. 7(a), 8(a), and 9(a)) do not account for rotor transmission loss and the swirl flow between the rotor and stator. These factors contribute to the
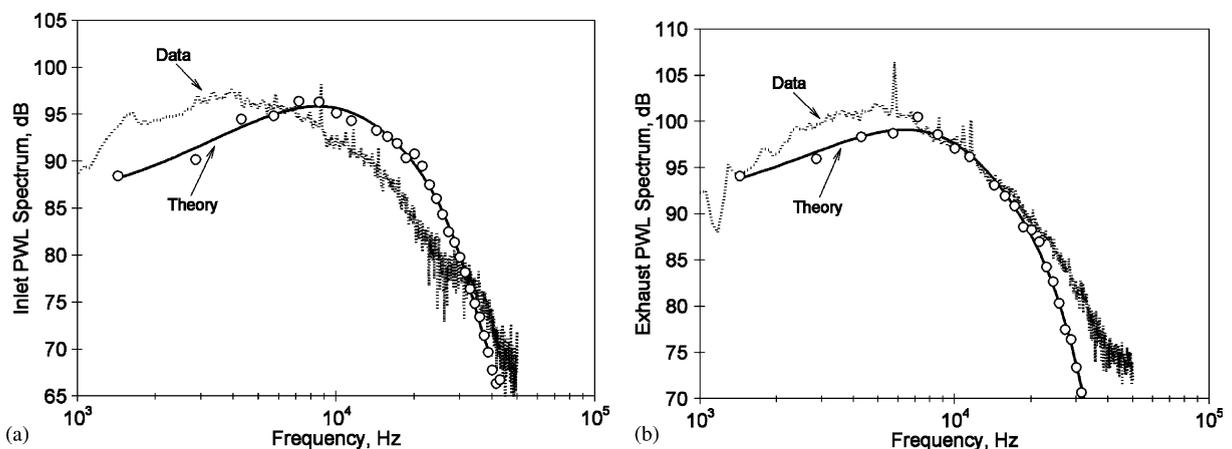

Fig. 7. Comparison of computed and measured spectra for the baseline stator (54 radial vanes) at approach: (a) inlet, (b) exhaust.
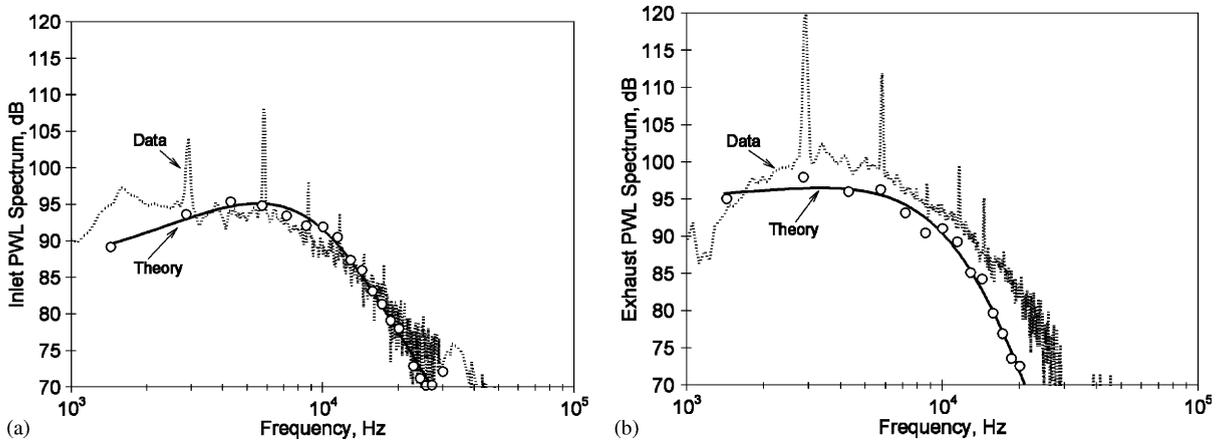
Fig. 8. Comparison of computed and measured spectra for the low-count stator (26 radial vanes) at approach: (a) inlet, (b) exhaust.
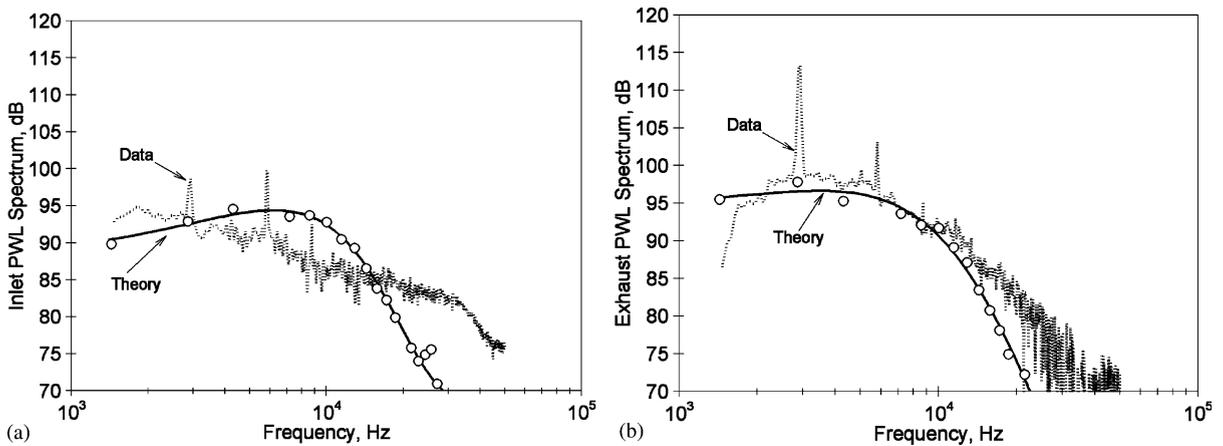

Fig. 9. Comparison of computed and measured spectra for the low-noise stator (26 swept vanes) at approach: (a) inlet, (b) exhaust.

large discrepancies observed (such as in Fig. 9(a)) between the measured and computed spectra. In the sections below, comparisons are shown only for the fan exhaust noise.

3.2. Effect of fan tip speed on spectra of acoustic power

The variation of acoustic power with fan tip speed is shown for the 54 radial vane configuration in Fig. 10. The predicted exhaust spectra of acoustic power for the three tip speeds of interest are shown in Fig. 10(a) and the measured spectra for the same conditions are shown in Fig. 10(b). The predicted spectra are seen to match the experimentally observed *trend* with the fan tip speed except at low frequencies where the measurements may include additional noise sources other
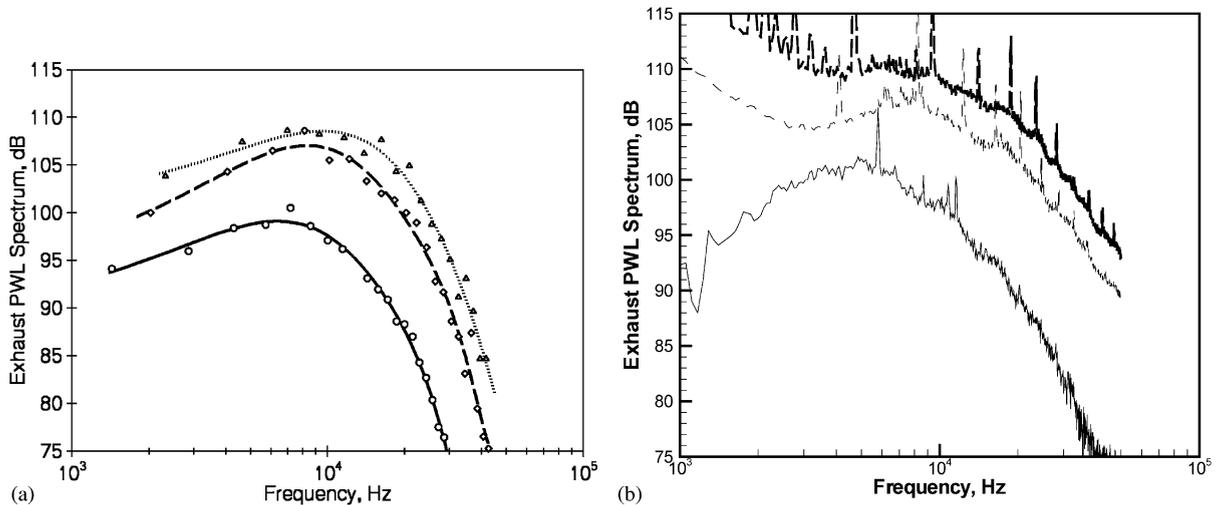
Fig. 10. Effect of fan tip speed on fan exhaust duct acoustic power spectrum for the baseline stator. (a) Computed spectra: solid line, approach; dashed line, cutback; and dotted line, takeoff. (b) Measured spectra: solid line, approach; dashed line, cutback; and long dashed line, takeoff.

than rotor wake turbulence noise (see also Ref. [13]). However, it is to be noted that the inlet/exhaust noise separation at higher speeds encountered problems as discussed in Section 2.3.

3.3. Variation of noise with vane count

As the vane count is reduced, the rotor-wake turbulence generated broadband noise is expected to reduce substantially. The cut-on fan design is expected to produce less broadband noise than the cut-off design to counteract the cut-on tone noise levels.

Fig. 11(a) shows computed exhaust power spectra for 54 radial vane and 26 radial vane configurations at approach and the corresponding measured spectra are shown in Fig. 11(b). It is seen that the experimentally observed noise reduction due to reduced vane count is clearly shown in the predictions. The acoustic power for 26 radial vanes is substantially lower than for the 54 radial vanes configuration. The power is expected to vary as $10 \log N_V^2$ (see Ref. [10]) where N_V is the vane count. This should result in 6.3 dB, (20 LOG (54/26)), reduction in power levels for the 26-vane OGV compared with the 54-vane OGV. The predicted reduction in power due to the reduction in vane number is higher than expected at high frequencies. At low frequencies (<3 kHz), the experimental result is insensitive to the vane count. The noise levels computed for the two configurations are not significantly different, probably because at low frequencies there are additional noise sources present, which are not modeled in the present theory. A similar trend with vane count was observed in Boeing broadband noise experiments on the effect of vane count on noise spectra [14].

The reduction in acoustic power level due to a reduction in vane count was further explored to understand the contributing factors, in an effort to explain the more than expected reduction in acoustic power. An examination of inputs and computed power levels indicated a strong dependence on the vane stagger angle. Fig. 12 shows the power levels of the exhaust approach
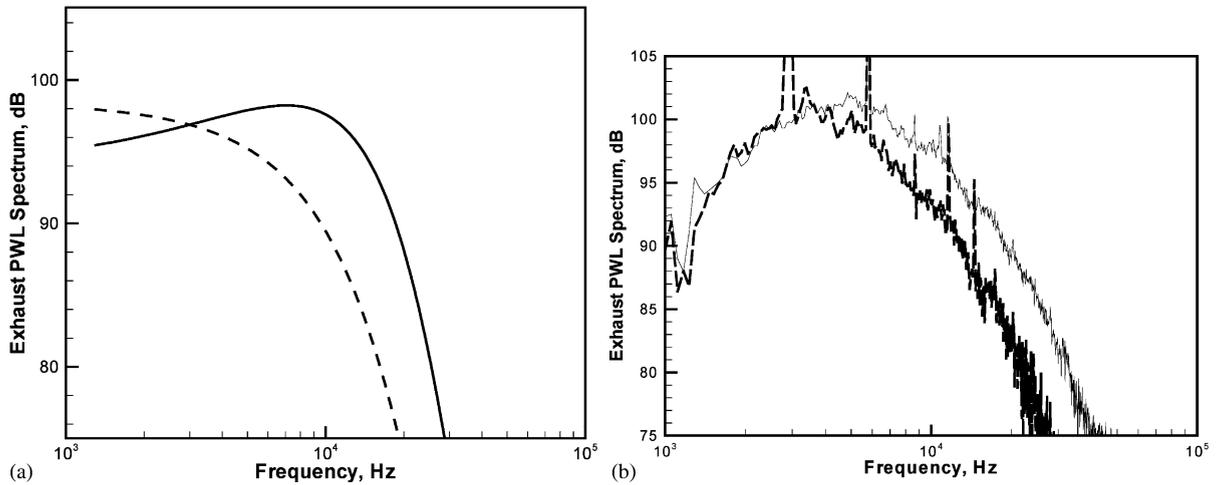
Fig. 11. Effect of vane count on exhaust acoustic power spectrum at approach. (a) Computed spectra: solid line, 54 radial vanes; dashed line, 26 radial vanes. (b) Measured spectra: solid line, 54 radial vanes; long dashed line, 26 radial vanes.
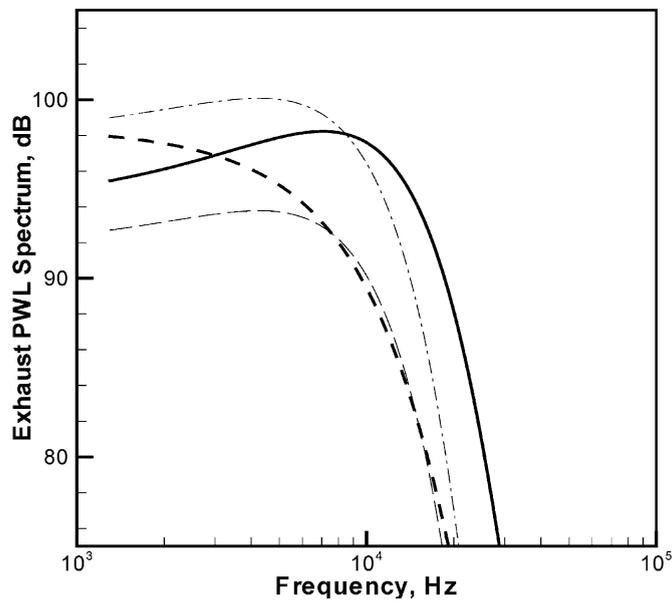

Fig. 12. Component contributions to 26-vane OGV power levels: solid line, 54-vane OGV; dashed line, 26-vane OGV; dash–dotted line, 54-vane case with the stagger angle of 26-vane case; long-dashed line, dash–dotted line minus 6.3 dB (20 log(54/26)).

condition as in Fig. 11, for 54 and 26 radial vanes. The third curve (dash–dotted one) is the power level obtained when the 54 radial vane stator stagger angle is replaced with that of 26 radial vane configuration. A substantial reduction in acoustic power at high frequencies is clearly seen. Now, if the 6.3 dB acoustic power reduction that would result from the vane count reduction from 54 to

26, is subtracted from the third curve, the fourth curve (long-dashed one) results. It is seen that at high frequencies, this curve and that for the 26 radial vane case (dashed one) are in close agreement suggesting that at least at high frequencies, in addition to the reduction in vane count, the stagger angle change contributes to the observed lower power level of the low vane count stator fan considered in the present study. At low frequencies (<3 kHz), while the experimental result is insensitive to the vane count, the prediction shows an increase with reduction in vane count. The reason for this switch in predicted power level variation at low frequencies is not clear.

3.4. Effect of vane sweep

Vane sweep has been found to result in substantial reduction in tone noise levels compared to the radial vane configuration [17]. The current broadband noise predictions do not show any decrease in acoustic power levels for the 26 swept geometry compared to the 26 vane radial (see Fig. 13(a)). Woodward [13] found that at certain fan speeds the vane sweep reduces the broadband noise by one to two decibels in addition to the reduction in tone noise. The measured spectra for the approach exhaust radiation shown in Fig. 13(b) show a small reduction in noise level in the low frequency range (<10 kHz) due to vane sweep. It should be emphasized here that if BPF tone harmonics are removed from the measured spectra the reduction due to vane sweep will be even smaller. In addition, Envia [18] showed that if all the shaft harmonics are removed, the swept vane average broadband levels are very close to the radial vane levels.

3.5. Acoustic power as a function of mode order m

The variations of modal power as a function of circumferential mode order m were studied for both the inlet and exhaust radiation. The modal power variation with m at the exhaust was
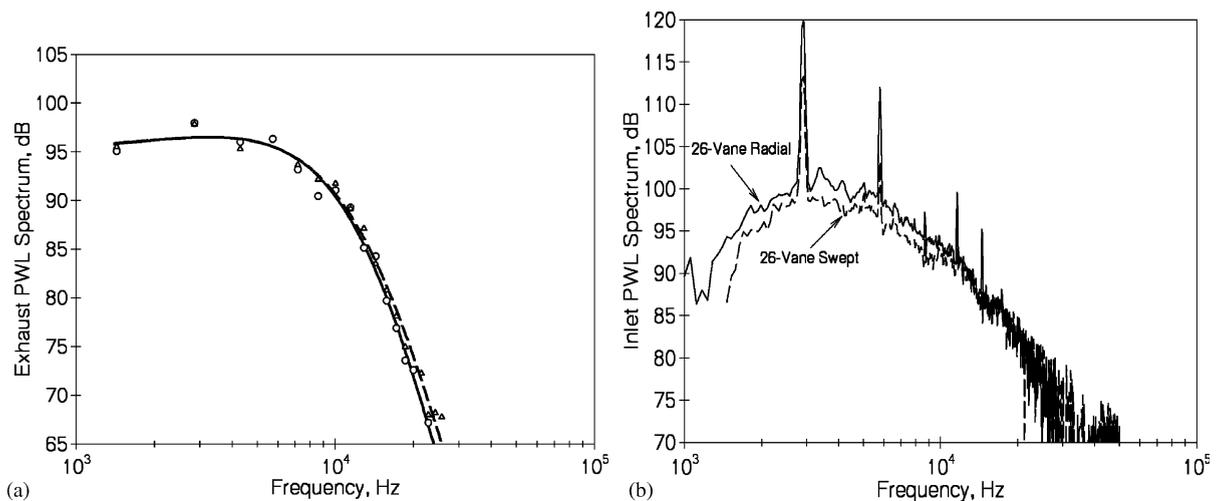

Fig. 13. Effect of vane sweep on exhaust acoustic power spectrum at approach. (a) Computed spectra: solid line, 26-radial vanes; dashed line, 26-swept vanes. (b) Measured spectra: solid line, 26-radial vane; long dashed line, 26-swept vanes.
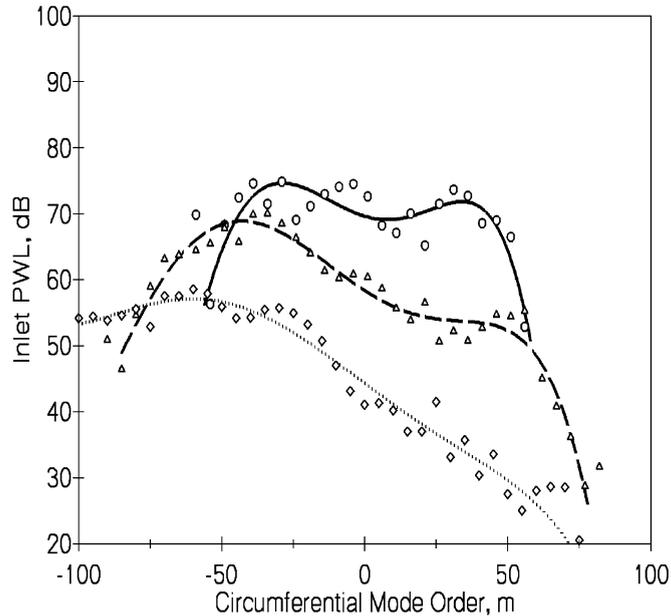
Fig. 14. Inlet acoustic power distribution as a function of spinning mode order (m) for the baseline stator at approach: solid line, 3BPF; dashed line, 5BPF; dotted line, 7BPF.

found to be similar to that at the inlet. Hence, the variation is illustrated here only for the inlet radiation.

Fig. 14 shows the inlet acoustic power as function of circumferential mode m order for frequencies from 3BPF, 5BPF and 7BPF. Note that the number of cut-on circumferential mode orders (m) and the number of cut-on radial mode orders (n) in each m-order increase linearly with frequency as shown in Fig. 15. Reverting to Fig. 14, the peak acoustic power level, in general, reduces with increases in frequency. At frequencies higher than 5BPF, the fall off with increasing m order is higher for the positive m orders than for negative m orders.

3.6. Cut-off ratio and acoustic power

Sometimes it is helpful to look at the acoustic power radiated as a function of cut-off ratio and that is particularly done in design and tradeoff studies [19,20]. Fig. 16 shows the variation of acoustic power as a function of cut-off ratio for inlet radiation at approach for two frequencies, 4BPF and 6BPF. The symbols denote different m orders and five n orders ($n = 0, \ldots, 4$) are included in the plot. Since no effect of flow swirl is included in the current model, the same number of corotating and contrarotating modes are cut-on at each frequency. The acoustic power decreases sharply as the cut-off ratio is increased and eventually reaches nearly a plateau beyond a cut-off ratio of three for both frequencies.
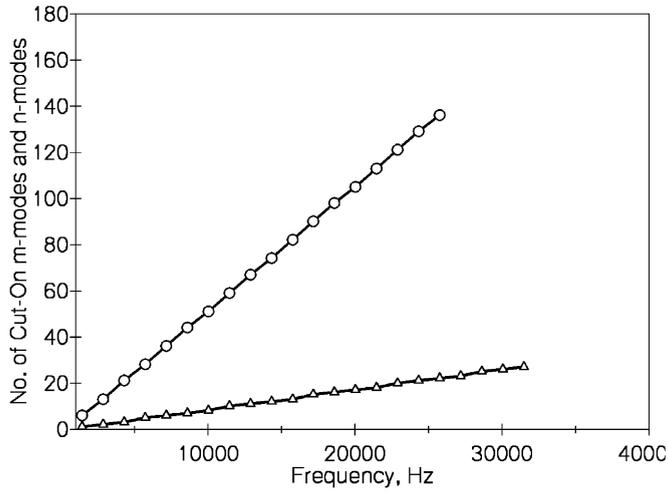
Fig. 15. Variation of the number of cut-on modes with frequency: circles, *m* orders; triangles, *n* orders. Baseline: approach.
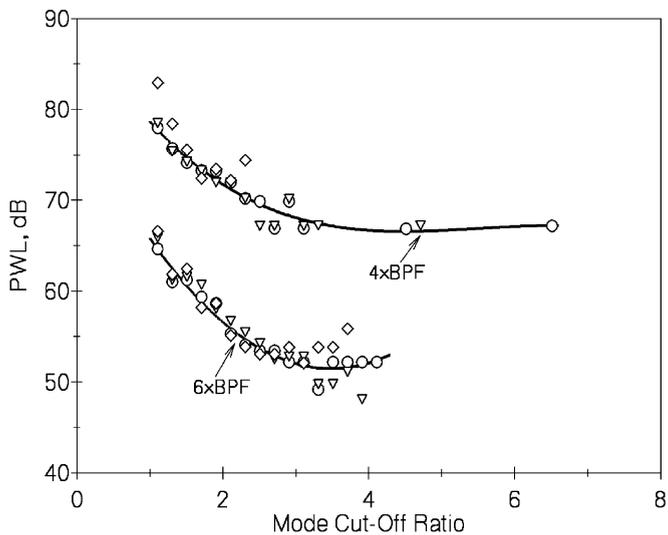

Fig. 16. Inlet acoustic power as a function of cut-off ratio for the baseline stator at approach.

4. Concluding remarks

The rotor wake turbulence stator interaction broadband noise has been computed for representative fan operating conditions for three fan stage configurations. The computations employ the wake flow turbulence information from accurate computational fluid dynamic solutions. The predicted noise spectra show the observed trends with fan tip speed and vane count. The predicted acoustic power levels and shape of the spectra show reasonable agreement

with the measured spectra for the exhaust noise at approach condition, where direct comparisons are possible.

Appendix A. Development of the broadband noise model

The stator broadband noise model used in this work is a blend of 2-D (strip) aerodynamics and 3-D (duct) acoustics. The unsteady response of the stator at each radius is calculated from an unrolled representation of the stator and incident rotor turbulent flow. As a result, radial gradients of the flow variables are ignored in the aerodynamic analysis and the dependence on the radius enters only parametrically in the unsteady response calculations. The acoustic analysis is, on the other hand, three-dimensional and allows for general classical duct mode representation of the broadband noise field. The formalism outlined here is based on the theory developed by Ventres et al. [10] and includes enhancements to allow for a more realistic description of the turbulence downstream of the fan. The crucial steps in the development of the underlying theory are shown below. However, important relations from Ref. [10] are often used as starting points in the interest of brevity. These are noted when used.

A.1. Rotor wake upwash turbulence model

In this analysis the blades and vanes are assumed to be zero thickness twisted flat plates that are lined up with the direction of the local mean flow at each radius. The unrolled geometry at an arbitrary radial slice is shown in Fig. 17. Let $w(\vec{x}, r, t)$ denote the fluctuating component of rotor wake velocity normal to the stator chord (i.e., the upwash) and $\langle w(\vec{x}, r_1, t)w^*(\vec{y}, r_2, \tau)\rangle$, its correlation function, both described in the stationary frame of reference. The wavenumber–frequency spectrum of the upwash is the Fourier transform of its correlation function given by

$$\langle \tilde{w}(\vec{k}, r_1, \omega)\tilde{w}^*(\vec{K}, r_2, v)\rangle = \int\int\int\int\int\int \langle w(\vec{x}, r_1, t)w^*(\vec{y}, r_2, \tau)\rangle \mathrm{e}^{-\mathrm{i}\vec{k}\cdot\vec{x}+\mathrm{i}\vec{K}\cdot\vec{y}+\mathrm{i}\omega t-\mathrm{i}v\tau}\,\mathrm{d}\vec{x}\,\mathrm{d}\vec{y}\,\mathrm{d}t\,\mathrm{d}\tau,$$

(A.1)

where $\langle\cdot\rangle$ denotes expected value. The description of the velocity correlation is more conveniently expressed in the rotating frame. The transformation between the two frames is given by

$$\vec{X} = \vec{x} + \vec{D} + (\Omega r_1 t)\hat{e}_2, \quad \vec{Y} = \vec{y} + \vec{D} + (\Omega r_2 \tau)\hat{e}_2,$$
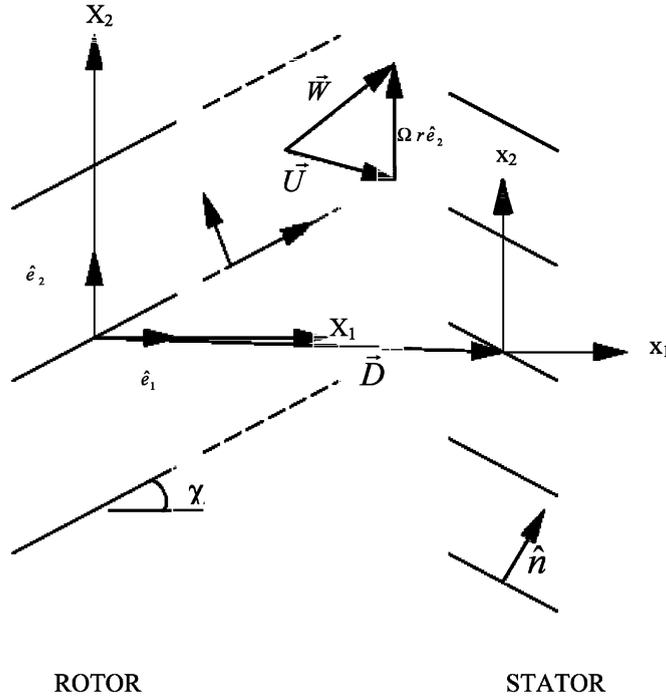
(A.2)

Fig. 17. Rotor–stator geometry definition.

where $\vec{D}$ is the distance between the reference rotor blade and the reference stator vane, and Ω the rotor rotational speed (see Fig. 17). Thus, in the rotating frame,

$$\langle \tilde{w}(\vec{k},r_1,\omega)\tilde{w}^*(\vec{K},r_2,v)\rangle = \int\int\int\int\int\int \langle w(\vec{X},r_1,t)w^*(\vec{Y},r_2,\tau)\rangle e^{-i(\vec{K}-\vec{k})\cdot\vec{D}}$$
$$\times e^{-i\vec{k}\cdot\vec{X}+i\vec{K}\cdot\vec{Y}+i(\omega+(\Omega r_1 t)k_2)t-i(v+(\Omega r_2\tau)K_2)\tau}\, d\vec{X}\, d\vec{Y}\, dt\, d\tau. \tag{A.3}$$

Assuming a frozen, stationary and isotropic model for turbulence, the correlation function can be approximated as

$$\langle w(\vec{X},r_1,t)w^*(\vec{Y},r_2,\tau)\rangle \approx \langle w(\vec{X}-\vec{W}t,r_1)w^*(\vec{Y}-\vec{W}\tau,r_2)\rangle, \tag{A.4}$$

where $W = \Omega\bar{r}$ is the local wheel speed. Note that owing to the 'frozen gust' assumption, the correlation depends on the $\vec{X}-\vec{W}t$ combination rather than $\vec{X}$ and t individually. Next, the following form for the upwash velocity is assumed:

$$w(\vec{X}-\vec{W}t,r) = F(\vec{X}\cdot\hat{n},r)g(\vec{X}-\vec{W}t,r), \tag{A.5}$$

so that

$$\langle w(\vec{X}-\vec{W}t,r_1)w^*(\vec{Y}-\vec{W}\tau,r_2)\rangle = F(\vec{X}\cdot\hat{n},\bar{r})F^*(\vec{Y}\cdot\hat{n},\bar{r})\Phi(\vec{X}-\vec{Y}-\vec{W}(t-\tau),\Delta r),$$
$$\Phi(\vec{X}-\vec{Y}-\vec{W}(t-\tau),\Delta r) = \langle g(\vec{X}-\vec{W}t,r_1)g^*(\vec{Y}-\vec{W}\tau,r_2)\rangle, \tag{A.6}$$

where $\hat{n}$ is the normal to the stator chord and $\Delta r = r_2 - r_1$. In simplifying Eq. (A.6), it is further assumed that the radial length scale of turbulence is small which means that the correlation is nonzero only inside a small radial strip within which r_1 and r_2 can be approximated by their average, $\bar{r}$. Note that only in the arguments of the F functions, r_1 and r_2 are approximated by their average. F basically represents the distribution of the rms turbulence intensity across the blade pitch, while Φ denotes normalized correlation (i.e., $\Phi(0, \bar{r}) \equiv 1$). Both F and Φ are necessarily periodic in the circumferential direction. This does not mean that the instantaneous random velocity is the same within each passage, but rather that its statistics are the same. Representing F by a Gaussian function, the periodicity requirement leads (via the Possion sum formula) to

$$F(\vec{X} \cdot \hat{n}, \bar{r}) = u'_b + \frac{N_B L_w u'_w}{2\pi\bar{r}} \sum_{m=-\infty}^{\infty} e^{\frac{-1}{4\pi}\left(\frac{mN_B L_w}{\bar{r}}\right)^2} e^{\left(\frac{imN_B}{\bar{r}\cos\chi}\vec{X}\cdot\hat{n}b\right)}, \tag{A.7}$$

where u'_b and u'_w, respectively, are the background and wake (peak) rms turbulence intensities, N_B the rotor blade count, L_w the 'width' of the Gaussian function describing the wake turbulence intensity distribution across the blade pitch and χ the rotor blade angle. The periodicity of Φ is denoted by

$$\Phi(\vec{X}, \Delta r) = \frac{1}{2\pi\bar{r}} \sum_{s=-\infty}^{\infty} \phi(X_1, \Delta r) e^{isX_2/\bar{r}}. \tag{A.8}$$

In view of the change of variable,

$$\vec{\xi} = \vec{X} - \vec{Y} - \vec{W}(t - \tau). \tag{A.9}$$

The time integrals in Eq. (A.3) can be carried out explicitly resulting in

$$\langle \tilde{w}(\vec{k}, \bar{r}, \omega)\tilde{w}^*(\vec{K}, \bar{r}, v)\rangle = (2\pi)^2 \delta(\omega - \vec{k} \cdot \vec{W} + \Omega\bar{r}k_2)\delta(v - \vec{k} \cdot \vec{W} + \Omega\bar{r}K_2)e^{-i(\vec{K}-\vec{k})\cdot\vec{D}}$$
$$\times \int \int \int \int F((\vec{\xi} + \vec{Y}) \cdot \hat{n}, \bar{r})F^*(\vec{Y} \cdot \hat{n}, \bar{r})$$
$$\times \Phi(\vec{\xi}, \Delta r)e^{-i\vec{k}\cdot\vec{\xi}+i(\vec{K}-\vec{k})\cdot\vec{Y}} \, d\vec{\xi} \, d\vec{Y}. \tag{A.10}$$

Noting that $\vec{U} = \vec{W} - (\Omega\bar{r})\hat{e}_2$ and substituting in the last equation for F and Φ from Eqs. (A.7) and (A.8), one obtains

$$\langle \tilde{w}(\vec{k}, \bar{r}, \omega)\tilde{w}^*(\vec{K}, \bar{r}, v)\rangle = \delta(\omega - \vec{k} \cdot \vec{U})\delta(v - \vec{k} \cdot \vec{U} + \Omega\bar{r}(K_2 - k_2))e^{-i(\vec{K}-\vec{k})\cdot\vec{D}}(\Psi_1 + \Psi_2 + \Psi_3),$$

$$\Psi_1 = \frac{(N_B L_w u'_w)^2}{2\pi\bar{r}^3} \sum_{m=-\infty}^{\infty} \sum_{\ell=-\infty}^{\infty} \sum_{s=-\infty}^{\infty} e^{-\frac{1}{4\pi}\left(\frac{mN_B L_w}{\bar{r}}\right)^2} e^{-\frac{1}{4\pi}\left(\frac{\ell N_B L_w}{\bar{r}}\right)^2}$$
$$\times \int \int \int \int e^{\left(\frac{imN_B}{\bar{r}\cos\chi}(\vec{\xi}+\vec{Y})\cdot\hat{n}\right)} e^{-\left(\frac{i\ell N_B}{\bar{r}\cos\chi}\vec{Y}\cdot\hat{n}\right)} \phi(\vec{\xi}, \Delta r) e^{is\xi_2/\bar{r}} e^{-i\vec{k}\cdot\vec{\xi}+i(\vec{K}-\vec{k})\cdot\vec{Y}} \, d\vec{\xi} \, d\vec{Y},$$

$$\Psi_2 = \frac{(N_B L_w u_b' u_w')}{\bar{r}^2} \sum_{m=-\infty}^{\infty} \sum_{s=-\infty}^{\infty} e^{-\frac{1}{4\pi}\left(\frac{mN_B L_w}{\bar{r}}\right)^2}$$

$$\times \int \int \int \int \left(e^{\left(\frac{imN_B}{\bar{r}\cos\chi}(\vec{\xi}+\vec{Y})\cdot\hat{n}\right)} + e^{-\left(\frac{imN_B}{\bar{r}\cos\chi}\vec{Y}\cdot\hat{n}\right)} \right) \phi(\vec{\xi}, \Delta r) e^{is\xi_2/\bar{r}} e^{-i\vec{k}\cdot\vec{\xi}+i(\vec{K}-\vec{k})\cdot\vec{Y}} \,d\vec{\xi}\,d\vec{Y},$$

$$\Psi_3 = \frac{2\pi u_b'^2}{\bar{r}} \sum_{s=-\infty}^{\infty} \int \int \int \int \phi(\vec{\xi}, \Delta r) e^{is\xi_2/\bar{r}} e^{-i\vec{k}\cdot\vec{\xi}+i(\vec{K}-\vec{k})\cdot\vec{Y}} \,d\vec{\xi}\,d\vec{Y}. \tag{A.11}$$

It should be noted that in Ref. [10], only the Ψ_1 term is considered since the background turbulence is not considered separately.

Carrying out the remaining four integrals yields

$$\langle \tilde{w}(\vec{k}, \bar{r}, \omega)\tilde{w}^*(\vec{K}, \bar{r}, v) \rangle = \underbrace{\langle \tilde{w}(\vec{k}, \bar{r}, \omega)\tilde{w}^*(\vec{K}, \bar{r}, v) \rangle_1}_{\text{wake turbulence auto-correlation}}$$

$$+ \underbrace{\langle \tilde{w}(\vec{k}, \bar{r}, \omega)\tilde{w}^*(\vec{K}, \bar{r}, v) \rangle_2}_{\text{wake/background turbulence cross-correlation}}$$

$$+ \underbrace{\langle \tilde{w}(\vec{k}, \bar{r}, \omega)\tilde{w}^*(\vec{K}, \bar{r}, v) \rangle_3}_{\text{background turbulence auto-correlation}},$$

$$\langle \tilde{w}(\vec{k}, \bar{r}, \omega)\tilde{w}^*(\vec{K}, \bar{r}, v) \rangle_1 = \frac{(2\pi)^2 (N_B L_w u_w')^2}{\bar{r}^3} \delta(\omega - \vec{k}\cdot\vec{U})$$

$$\times \sum_{m=-\infty}^{\infty} \sum_{\ell=-\infty}^{\infty} \sum_{s=-\infty}^{\infty} e^{-\frac{1}{4\pi}\left(\frac{mN_B L_w}{\bar{r}}\right)^2} e^{-\frac{1}{4\pi}\left(\frac{\ell N_B L_w}{\bar{r}}\right)^2}$$

$$\times e^{i\left(\frac{(m-\ell)N_B}{\bar{r}\cos\chi}\right)\vec{D}\cdot\hat{n}} \tilde{\phi}\left(\vec{k} - \frac{mN_B}{\bar{r}\cos\chi}n_1, \Delta r\right) \delta\left((\vec{K}-\vec{k}) + \frac{(m-\ell)N_B}{\bar{r}\cos\chi}\hat{n}\right)$$

$$\times \delta\left(k_2 - \frac{(mN_B+s)}{\bar{r}}\right)\delta(v - \omega - \Omega(m-\ell)N_B),$$

$$\langle \tilde{w}(\vec{k}, \bar{r}, \omega)\tilde{w}^*(\vec{K}, \bar{r}, v) \rangle_2 = \frac{(2\pi)^3 N_B L_w u_b' u_w'}{\bar{r}^2} \delta(\omega - \vec{k}\cdot\vec{U}) \sum_{m=-\infty}^{\infty} \sum_{s=-\infty}^{\infty} e^{-\frac{1}{4\pi}\left(\frac{mN_B L_w}{\bar{r}}\right)^2}$$

$$\times \left\{ e^{i\left(\frac{mN_B}{\bar{r}\cos\chi}\right)\vec{D}\cdot\hat{n}} \tilde{\phi}\left(\vec{k} - \frac{mN_B}{\bar{r}\cos\chi}n_1, \Delta r\right) \delta\left((\vec{K}-\vec{k}) + \frac{mN_B}{\bar{r}\cos\chi}\hat{n}\right) \right.$$

$$\times \delta\left(k_2 - \frac{(mN_B+s)}{\bar{r}}\right) + e^{-i\left(\frac{mN_B}{\bar{r}\cos\chi}\right)\vec{D}\cdot\hat{n}} \tilde{\phi}(\vec{k}, \bar{r})$$

$$\left. \times \delta\left((\vec{K}-\vec{k}) - \frac{mN_B}{\bar{r}\cos\chi}\hat{n}\right)\delta\left(k_2 - \frac{s}{\bar{r}}\right)\right\}\delta(v - \omega - \Omega mN_B),$$

$$\langle \tilde{w}(\vec{k}, \bar{r}, \omega)\tilde{w}^*(\vec{K}, \bar{r}, v)\rangle_3 = \frac{(2\pi)^4 u_b'^2}{\bar{r}}\delta(\omega - \vec{k}\cdot\vec{U})$$
$$\times \sum_{s=-\infty}^{\infty} \tilde{\phi}(\vec{k}, \Delta r)\boldsymbol{\delta}(\vec{K} - \vec{k})\delta\left(k_2 - \frac{s}{\bar{r}}\right)\delta(v - \omega), \qquad (A.12)$$

where $\tilde{\phi}$ is the Fourier transform of ϕ. In deriving these equations use is made of the restrictions imposed by the argument of the vector Dirac delta functions to make further substitutions.

A.2. Duct mode rms pressure spectrum

The ensemble-averaged spectrum of the (m, n)th duct mode is given in Ref. [10] as

$$\langle \tilde{p}_{mn}(\omega)\tilde{p}_{mn}^*(v)\rangle = \frac{1}{4\Gamma^2 k_{mn}(\omega)k_{mn}(v)}$$
$$\times \int_{r_H}^{r_T}\int_{r_H}^{r_T}\int_{-b}^{b}\int_{-b}^{b} R(r_1, \omega)R(r_2, v)e^{i\mu(r_1,\omega)z_1}e^{-i\mu(r_2,v)z_2}$$
$$\times \left\{\sum_{j=0}^{N_V-1} e^{2i\pi mj/N_V}\sum_{\ell=0}^{N_V-1} e^{-2i\pi m\ell/N_V}\langle\Delta\tilde{p}_j(r_1, z_1, \omega)\Delta\tilde{p}_\ell^*(r_2, z_2, v)\rangle\right\}$$
$$\times dz_2\, dz_1\, dr_2\, dr_1, \qquad (A.13)$$

where R and μ are given by

$$R(r, \omega) = \left(\frac{m}{r}\cos\alpha + \gamma_{mn}(\omega)\sin\alpha\right)\psi_m(\kappa_{mn}r),$$
$$\mu(r, \omega) = -\frac{m}{r}\sin\alpha + \gamma_{mn}(\omega)\cos\alpha, \qquad (A.14)$$

and where ψ_m the duct mode, α is the vane stagger angle, κ_{mn} is the mode eigenvalue and $\Gamma = \pi(r_T^2 - r_H^2)$. Here, γ_{mn} and k_{mn} denote, respectively, the axial wavenumber of the duct mode with and without the convective correction. The expression $\langle\Delta\tilde{p}_j(z_1, r_1, \omega)\Delta\tilde{p}_\ell^*(z_2, r_2, v)\rangle$ is the expected value of the surface pressure spectrum on a single vane which is given by [10]

$$\langle\Delta\tilde{p}_j(z_1, r_1, \omega)\Delta\tilde{p}_\ell^*(z_2, r_2, v)\rangle = \frac{1}{(2\pi)^4}(\rho_0 U)^2 \int\int\int\int \wp(\vec{k}, z_1, r_1, \omega)\,\wp^*(\vec{K}, z_2, r_2, v)$$
$$\times \langle\tilde{w}(\vec{k}, r_1, \omega)\tilde{w}^*(\vec{K}, r_2, v)\rangle e^{ij\vec{k}.\vec{h}}e^{-i\ell\vec{K}.\vec{h}}\, d\vec{k}\, d\vec{K}, \qquad (A.15)$$

where $\wp(\vec{k}, z, r, \omega)$ denotes the chordwise pressure distribution due to unit upwash on the wavenumber–frequency basis. The sum of contributions from all vanes, i.e., the quantity in the curly brackets in Eq. (A.13), can be written as

$$\mathfrak{I} = \left\{\sum_{j=0}^{N_V-1} e^{2i\pi mj/N_V}\sum_{\ell=0}^{N_V-1} e^{-2i\pi m\ell/N_V}\langle\Delta\tilde{p}_j(z_1, r_1, \omega)\Delta\tilde{p}_\ell^*(z_2, r_2, v)\rangle\right\}$$

$$= \frac{1}{(2\pi)^4} (\rho_0 U)^2 \int \int \int \int \wp(\vec{k}, z_1, r_1, \omega) \wp^*(\vec{K}, z_2, r_2, v)$$

$$\times \sum_{j=0}^{N_V-1} e^{\mathrm{i}j(2\pi m/N_V + \vec{k}.\vec{h})} \sum_{\ell=0}^{N_V-1} e^{-\mathrm{i}\ell(2\pi m/N_V + \vec{K}.\vec{h})}$$

$$\times \langle \tilde{w}(\vec{k}, r_1, \omega)\tilde{w}^*(\vec{K}, r_2, v)\rangle \, \mathrm{d}\vec{k} \, \mathrm{d}\vec{K}. \tag{A.16}$$

Once again restricting the analysis to small radial integral scales, each of the (r_1, r_2) pairs can be replaced with their average value, $\bar{r}$, in Eqs. (A.16) and (A.12) can be used to substitute for $\langle \tilde{w}(\vec{k}, \bar{r}, \omega)\tilde{w}^*(\vec{K}, \bar{r}, v)\rangle$. In evaluating the resulting integrals, use is made of the restrictions imposed by the arguments of the various Dirac delta functions in Eq. (A.12) which, in particular, yield

$$k_2 = \frac{(m_1 N_B + s)}{\bar{r}}, \quad K_2 = \frac{(\ell_1 N_B + s)}{\bar{r}} \quad \text{for } \langle\cdot\rangle_1,$$

$$k_2, K_2 = \frac{(m_1 N_B + s)}{\bar{r}}, \quad K_2, k_2 = \frac{s}{\bar{r}} \quad \text{for } \langle\cdot\rangle_2,$$

$$k_2 = \frac{s}{\bar{r}}, \quad K_2 = \frac{s}{\bar{r}} \quad \text{for } \langle\cdot\rangle_3. \tag{A.17}$$

Furthermore, these relations imply

$$\vec{k} \cdot \vec{h} = k_2 h = \frac{2\pi(m_1 N_B + s)}{N_V}, \quad \vec{K} \cdot \vec{h} = K_2 h = \frac{2\pi(\ell_1 N_B + s)}{N_V},$$

$$\sum_{j=0}^{N_V-1} e^{\mathrm{i}j(2\pi m/N_V + \vec{k}.\vec{h})} = \begin{cases} N_V & \text{if } m + s + m_1 N_B = p_1 N_V \\ 0 & \text{otherwise} \end{cases} \quad \text{for } \langle\cdot\rangle_1,$$

$$\sum_{\ell=0}^{N_V-1} e^{-\mathrm{i}\ell(2\pi m/N_V + \vec{K}.\vec{h})} = \begin{cases} N_V & \text{if } m + s + \ell_1 N_B = q_1 N_V, \\ 0 & \text{otherwise}, \end{cases}$$

$$\vec{k} \cdot \vec{h} = k_2 h = \frac{2\pi(m_1 N_B + s)}{N_V}, \quad \vec{K} \cdot \vec{h} = K_2 h = \frac{2\pi s}{N_V},$$

$$\sum_{j=0}^{N_V-1} e^{\mathrm{i}j(2\pi m/N_V + \vec{k}.\vec{h})} = \begin{cases} N_V & \text{if } m + s + m_1 N_B = p_1 N_V \\ 0 & \text{otherwise} \end{cases} \quad \text{for } \langle\cdot\rangle_2,$$

$$\sum_{\ell=0}^{N_V-1} e^{-\mathrm{i}\ell(2\pi m/N_V + \vec{K}.\vec{h})} = \begin{cases} N_V & \text{if } m + s = q_1 N_V, \\ 0 & \text{otherwise}, \end{cases}$$

$$\vec{k} \cdot \vec{h} = k_2 h = \frac{2\pi s}{N_V}, \quad \vec{K} \cdot \vec{h} = K_2 h = \frac{2\pi s}{N_V},$$

$$\sum_{j=0}^{N_V-1} \mathrm{e}^{\mathrm{i}j(2\pi m/N_V + \vec{k}.\vec{h})} = \begin{cases} N_V & \text{if } m+s = p_1 N_V \\ 0 & \text{otherwise} \end{cases} \quad \text{for } \langle \cdot \rangle_3,$$

$$\sum_{\ell=0}^{N_V-1} \mathrm{e}^{-\mathrm{i}\ell(2\pi m/N_V + \vec{K}.\vec{h})} = \begin{cases} N_V & \text{if } m+s = q_1 N_V, \\ 0 & \text{otherwise}. \end{cases} \tag{A.18}$$

Consider the first element of Eq. (A.18). It implies the relation $(m_1 - \ell_1)N_B = (p_1 - q_1)N_V$. For arbitrary choices of integers m_1 and ℓ_1, there can only be integer solutions to this relationship if $(p_1 - q_1) = jB$ which in turn implies $(m_1 - \ell_1) = jN_V$. Setting $\ell_1 = m_1 - jN_V$, yields $s = q_1 N_V - m_1 N_B + jN_B N_V - m$. The summations over the indices s and ℓ_1 can therefore be replaced by the summations over the indices pair j and q_1. Similar arguments for the remaining two elements lead to similar conclusions. With this change of indices, the substitution of $\langle \tilde{w}(\vec{k}, \vec{r}, \omega) \tilde{w}^*(\vec{K}, \vec{r}, v) \rangle$ from Eq. (A.12) in Eq. (A.16) yields

$$\begin{aligned}
\mathfrak{I}_1 = {} & \frac{(\rho_0 U N_V)^2 (N_B L_w u'_w)^2}{(2\pi)^2 \bar{r}^3} \sum_{m_1=-\infty}^{\infty} \sum_{q_1=-\infty}^{\infty} \sum_{j=-\infty}^{\infty} \mathrm{e}^{-\frac{1}{4\pi}\left(\frac{m_1 N_B L_w}{\bar{r}}\right)^2} \\
& \times \mathrm{e}^{-\frac{1}{4\pi}\left(\frac{(m_1 - jN_V)N_B L_w}{\bar{r}}\right)^2} \mathrm{e}^{\mathrm{i}\left(\frac{jN_B N_V}{\bar{r}\cos\chi}\right)\vec{D}\cdot\hat{n}} \\
& \times \int\int\int\int \wp(\vec{k}, z_1, \bar{r}, \omega) \, \wp^*(\vec{K}, z_2, \bar{r}, v)\delta(\omega - \vec{k}\cdot\vec{U}) \\
& \times \tilde{\phi}\left(\vec{k} - \frac{mN_B}{\bar{r}\cos\chi}\hat{n}, \Delta r\right)\boldsymbol{\delta}\left((\vec{K} - \vec{k}) + \frac{jN_B N_V}{\bar{r}\cos\chi}\hat{n}\right) \\
& \times \delta\left(k_2 - \frac{(q_1 N_V + jN_B N_V - m)}{\bar{r}}\right) \\
& \times \delta(v - \omega - jN_B N_V \Omega) \, \mathrm{d}\vec{k}\,\mathrm{d}\vec{K},
\end{aligned}$$

$$\begin{aligned}
\mathfrak{I}_2 = {} & \frac{(\rho_0 U N_V)^2 N_B L_w u'_b u'_w}{2\pi \bar{r}^2} \sum_{m_1=-\infty}^{\infty} \sum_{q_1=-\infty}^{\infty} \mathrm{e}^{-\frac{1}{4\pi}\left(\frac{m_1 N_B L_w}{\bar{r}}\right)^2} \\
& \times \int\int\int\int \wp(\vec{k}, z_1, \bar{r}, \omega) \, \wp^*(\vec{K}, z_2, \bar{r}, v)\delta(\omega - \vec{k}\cdot\vec{U})\delta(v - \omega - m_1 N_B \Omega) \\
& \times \left\{ \mathrm{e}^{\mathrm{i}\left(\frac{m_1 N_V}{\bar{r}\cos\chi}\right)\vec{D}\cdot\hat{n}} \tilde{\phi}\left(\vec{k} - \frac{mN_B}{\bar{r}\cos\chi}\hat{n}, \Delta r\right)\boldsymbol{\delta}\left((\vec{K} - \vec{k}) + \frac{m_1 N_B}{\bar{r}\cos\chi}\hat{n}\right) \right. \\
& \times \delta\left(k_2 - \frac{q_1 N_V + m_1 N_B - m}{\bar{r}}\right) + \mathrm{e}^{-\mathrm{i}\left(\frac{m_1 N_V}{\bar{r}\cos\chi}\right)\vec{D}\cdot\hat{n}} \tilde{\phi}(\vec{k}, \Delta r) \\
& \left. \times \boldsymbol{\delta}\left((\vec{K} - \vec{k}) - \frac{m_1 N_B}{\bar{r}\cos\chi}\hat{n}\right)\delta\left(k_2 - \frac{q_1 N_V - m}{\bar{r}}\right) \right\} \mathrm{d}\vec{k}\,\mathrm{d}\vec{K},
\end{aligned}$$

$$\Im_3 = \frac{(\rho_0 U N_V)^2 u_b'^2}{\bar{r}} \sum_{q_1=-\infty}^{\infty} \int \int \int \int \wp(\vec{k}, z_1, \bar{r}, \omega) \wp^*(\vec{K}, z_2, \bar{r}, v) \delta(\omega - \vec{k} \cdot \vec{U})$$

$$\times \tilde{\phi}(\vec{k}, \Delta r) \delta(\vec{K} - \vec{k}) \delta\left(k_2 - \frac{q_1 N_V - m}{\bar{r}}\right) \delta(v - \omega) \, d\vec{k} \, d\vec{K}. \tag{A.19}$$

The sums over the index j in $\Im_1$ and over the index m_1 in $\Im_2$ represents fluctuating power terms that would integrate to zero when averaged. Therefore, one only need consider $j, m_1 = 0$ terms. Integrating the resulting expression over the wavenumbers $\vec{k}$ and $\vec{K}$ yields

$$\Im_1 = \frac{(\rho_0 U N_V)^2 (N_B L_w u_w')^2}{(2\pi)^2 \bar{r}^3} \delta(v - \omega) \sum_{m_1=-\infty}^{\infty} \sum_{q_1=-\infty}^{\infty} \left| e^{-\frac{1}{4\pi}\left(\frac{m_1 N_B L_w}{\bar{r}}\right)^2} \right|^2$$

$$\times \wp(\vec{k}, z_1, \bar{r}, \omega) \wp^*(\vec{k}, z_2, \bar{r}, v) \tilde{\phi}\left(\vec{k} - \frac{m N_B}{\bar{r} \cos \chi} \hat{n}, \Delta r\right),$$

$$\Im_2 = \frac{(\rho_0 U N_V)^2 N_B L_w u_b' u_w'}{2\pi \bar{r}^2} \delta(v - \omega) \sum_{q_1=-\infty}^{\infty} e^{-\frac{1}{4\pi}\left(\frac{m_1 N_B L_w}{\bar{r}}\right)^2}$$

$$\times \wp(\vec{k}, z_1, \bar{r}, \omega) \wp^*(\vec{k}, z_2, \bar{r}, v) \left\{ \tilde{\phi}\left(\vec{k} - \frac{m N_B}{\bar{r} \cos \chi} \hat{n}, \Delta r\right) + \tilde{\phi}(\vec{k}, \Delta r) \right\},$$

$$\Im_3 = \frac{(\rho_0 U N_V)^2 u_b'^2}{\bar{r}} \delta(v - \omega) \sum_{q_1=-\infty}^{\infty} \wp(\vec{k}, z_1, \bar{r}, \omega) \wp^*(\vec{k}, z_2, \bar{r}, v) \tilde{\phi}(\vec{k}, \Delta r), \tag{A.20}$$

where now $\vec{k}$ denotes a vector with components $k_1 = \omega/U_1 - k_2 U_2/U_1$ and $k_2 = (q_1 N_V - m)/\bar{r}$. Ignoring steady loading effects, the vane unsteady pressure distribution $\wp(\vec{k}, z, \bar{r}, \omega)$ can be approximated by its chordwise contribution $\wp(k_z, z, \bar{r}, \omega)$ if the vanes are assumed to be aligned with the direction of the local mean flow velocity $\vec{U}$. Under this approximation $\wp(k_z, z, \bar{r}, \omega)$ is independent of indices of the various sums and thus can be moved out from under the double summation sign. The result is

$$\Im = \Im_1 + \Im_2 + \Im_3 = (\rho_0 U N_V)^2 \delta(v - \omega) \wp(k_z, z_1, \bar{r}, \omega) \wp^*(k_z, z_2, \bar{r}, v)$$

$$\times \left\{ \frac{(N_B L_w u_w')^2}{(2\pi)^2 \bar{r}^3} \sum_{m_1=-\infty}^{\infty} \sum_{q_1=-\infty}^{\infty} \left| e^{-\frac{1}{4\pi}\left(\frac{m_1 B L_w}{\bar{r}}\right)^2} \right|^2 \tilde{\phi}\left(\vec{k} - \frac{m N_B}{\bar{r} \cos \chi} \hat{n}, \Delta r\right) \right.$$

$$+ \frac{N_B L_w u_b' u_w'}{2\pi \bar{r}^2} \sum_{q_1=-\infty}^{\infty} e^{-\frac{1}{4\pi}\left(\frac{m_1 N_B L_w}{\bar{r}}\right)^2}$$

$$\times \left[\tilde{\phi}\left(\vec{k} - \frac{m N_B}{\bar{r} \cos \chi} \hat{n}, \Delta r\right) + \tilde{\phi}(\vec{k}, \Delta r) \right] + \frac{u_b'^2}{\bar{r}} \sum_{q_1=-\infty}^{\infty} \tilde{\phi}(\vec{k}, \Delta r) \right\}. \tag{A.21}$$

The per mode spectrum is thus reduced to

$$
\langle \tilde{p}(\omega)\tilde{p}^*(v) \rangle = \frac{1}{4\Gamma^2 k_{mn}(\omega)k_{mn}(v)} \int_{r_H}^{r_T} \int_{r_H}^{r_T} \{\Im\} \psi_m(\kappa_{mn}\bar{r})|_\omega \psi_m(\kappa_{mn}\bar{r})|_v
$$
$$
\times b^2 \left(\frac{m}{\bar{r}}\cos\alpha + \gamma_{mn}(\omega)\sin\alpha\right) \left(\frac{m}{\bar{r}}\cos\alpha + \gamma_{mn}(v)\sin\alpha\right)
$$
$$
\times C_{mn}(\bar{r},\omega)C_{mn}^*(\bar{r},v)\,\mathrm{d}(\Delta r)\,\mathrm{d}\bar{r}, \tag{A.22}
$$

where

$$
C_{mn}(\bar{r},\omega) = \frac{1}{b}\int_{-b}^{b} \wp(\bar{r},z,k_z,\omega)\mathrm{e}^{\mathrm{i}\mu(\bar{r},\omega)z}\,\mathrm{d}z,
$$

and where the approximation $\mathrm{d}r_1\,\mathrm{d}r_2 \approx \mathrm{d}(\Delta r)\,\mathrm{d}\bar{r}$ is used in view of the smallness of the radial integral length scales. Note that the chordwise variations of the unsteady pressure on the vane is taken into account via the chordwise integral $C_{mn}(\bar{r},\omega)$. It remains to model $\tilde{\phi}$ in Eq. (A.21) so as to complete the calculation of the expected mode spectrum.

In order to make the problem tractable, a multiplicative structure for the correlation function ϕ is assumed with corresponding integral length scales in the three principal directions. Thus

$$
\phi(\vec{\xi},\Delta r) = \phi_1(\xi_1/L_1)\phi_2(\xi_2/L_2)\phi_r(\Delta r/L_r), \tag{A.23}
$$

where the length scale in each direction is defined as $L = \int \phi(x)\,\mathrm{d}x$. Indices 1 and 2 from now on refer to directions along and normal to the vane chord. The integral lengths scales L_1, L_2 and L_r can be obtained from suitable turbulence data (or from numerical solutions as in the present paper). For the purposes of this work a Gaussian form is assumed for each of the correlation functions ϕ_1, ϕ_2 and ϕ_r. Taking the Fourier transform of Eq. (A.23) yields

$$
\tilde{\phi}(\vec{\lambda},\Delta r) = L_1 L_2 \tilde{\phi}_1(\lambda_1 L_1)\tilde{\phi}_2(\lambda_2 L_2)\phi_r(\Delta r/L_r). \tag{A.24}
$$

For $\tilde{\phi}(\vec{k} - (mN_B/\bar{r}\cos\chi)\hat{n},\Delta r)$, which is associated with the wake turbulence, the components of the 'wavenumber' $\vec{\lambda}$ are given by

$$
\lambda_1^{(w)} = \frac{\omega + m_1 N_B\Omega}{U_1} - \frac{U_2}{U_1}\left(\frac{q_1 N_V - m_1 N_B - m}{\bar{r}}\right) \approx \frac{\omega + m_1 N_B\Omega}{U_1},
$$
$$
\lambda_2^{(w)} = \frac{q_1 N_V - m_1 N_B - m}{\bar{r}}, \tag{A.25}
$$

where, consistent with flat plate cascade response model used in this work, the transverse component of the mean flow, i.e., U_2, has been neglected. The components of $\vec{\lambda}$ for $\tilde{\phi}(\vec{k},\Delta r)$, which is associated with the background turbulence, are given by

$$
\lambda_1^{(b)} = \frac{\omega - q_1 N_V + m}{U_1}, \quad \lambda_2^{(b)} = \frac{q_1 N_V - m}{\bar{r}}. \tag{A.26}
$$

Substituting for $\Im$ in Eq. (A.22) and carrying out the integration over Δr yields

$$
\begin{aligned}
\langle \tilde{p}(\omega)\tilde{p}^*(v)\rangle = & \left(\tfrac{1}{2}\rho_0 N_V\right)^2 \left\{ \frac{\delta(v-\omega)}{\Gamma^2 k_{mn}(\omega)k_{mn}(v)} \right\} \int_{r_H}^{r_T} \psi_m(\kappa_{mn}r)|_\omega \psi_m(\kappa_{mn}r)|_v (U_1 b)^2 L_r \\
& \times \left(\frac{m}{\bar{r}}\cos\alpha + \gamma_{mn}(\omega)\sin\alpha \right) \left(\frac{m}{\bar{r}}\cos\alpha + \gamma_{mn}(v)\sin\alpha \right) C_{mn}(\bar{r},\omega) C_{mn}^*(\bar{r},v) \\
& \times \left\{ \frac{(N_B L_w u_w')^2}{(2\pi)^2 \bar{r}^3} \sum_{m_1=-\infty}^{\infty} \sum_{q_1=-\infty}^{\infty} \left(e^{-\frac{1}{4\pi}\left(\frac{m_1 N_B L_w}{\bar{r}}\right)^2} \right)^2 L_1^{(w)} L_2^{(w)} \tilde{\phi}_1\left(\lambda_1^{(w)} L_1^{(w)}\right) \tilde{\phi}_2\left(\lambda_2^{(w)} L_2^{(w)}\right) \right. \\
& + \frac{N_B L_w u_b' u_w'}{2\pi \bar{r}^2} \sum_{q_1=-\infty}^{\infty} e^{-\frac{1}{4\pi}\left(\frac{m_1 N_B L_w}{\bar{r}}\right)^2} \left[L_1^{(w)} L_2^{(w)} \tilde{\phi}_1\left(\lambda_1^{(w)} L_1^{(w)}\right) \tilde{\phi}_2\left(\lambda_2^{(w)} L_2^{(w)}\right) \right. \\
& \left. + L_1^{(b)} L_2^{(b)} \tilde{\phi}_1\left(\lambda_1^{(b)} L_1^{(b)}\right) \tilde{\phi}_2\left(\lambda_2^{(b)} L_2^{(b)}\right) \right] + \frac{u_b'^2}{\bar{r}} \sum_{q_1=-\infty}^{\infty} L_1^{(b)} L_2^{(b)} \tilde{\phi}_1\left(\lambda_1^{(b)} L_1^{(b)}\right) \tilde{\phi}_2\left(\lambda_2^{(b)} L_2^{(b)}\right) \right\} d\bar{r}.
\end{aligned}
$$
(A.27)

In theory, the integral length scales for the background and wake turbulence can be different, but for the purposes of this work they are taken to be the same:

$$
\begin{aligned}
\langle \tilde{p}(\omega)\tilde{p}^*(v)\rangle = & \left(\tfrac{1}{2}\rho_0 N_V\right)^2 \left\{ \frac{\delta(v-\omega)}{\Gamma^2 k_{mn}(\omega)k_{mn}(v)} \right\} \int_{r_H}^{r_T} \psi_m(\kappa_{mn}r)|_\omega \psi_m(\kappa_{mn}r)|_v (U_1 b)^2 L_r \\
& \times \left(\frac{m}{\bar{r}}\cos\alpha + \gamma_{mn}(\omega)\sin\alpha \right) \left(\frac{m}{\bar{r}}\cos\alpha + \gamma_{mn}(v)\sin\alpha \right) C_{mn}(\bar{r},\omega) C_{mn}^*(\bar{r},v) \\
& \times \left\{ \frac{(N_B L_w u_w')^2}{(2\pi)^2 \bar{r}^3} \sum_{m_1=-\infty}^{\infty} \sum_{q_1=-\infty}^{\infty} \left(e^{-\frac{1}{4\pi}\left(\frac{m_1 N_B L_w}{\bar{r}}\right)^2} \right)^2 L_1 L_2 \tilde{\phi}_1\left(\lambda_1^{(w)} L_1\right) \tilde{\phi}_2\left(\lambda_2^{(w)} L_2\right) \right. \\
& + \frac{N_B L_w u_b' u_w'}{2\pi \bar{r}^2} \sum_{q_1=-\infty}^{\infty} e^{-\frac{1}{4\pi}\left(\frac{m_1 N_B L_w}{\bar{r}}\right)^2} \left[L_1 L_2 \tilde{\phi}_1\left(\lambda_1^{(w)} L_1\right) \tilde{\phi}_2\left(\lambda_2^{(w)} L_2\right) \right. \\
& \left. + L_1 L_2 \tilde{\phi}_1\left(\lambda_1^{(b)} L_1\right) \tilde{\phi}_2\left(\lambda_2^{(b)} L_2\right) \right] + \frac{u_b'^2}{\bar{r}} \sum_{q_1=-\infty}^{\infty} L_1 L_2 \tilde{\phi}_1\left(\lambda_1^{(b)} L_1\right) \tilde{\phi}_2\left(\lambda_2^{(b)} L_2\right) \right\} d\bar{r}.
\end{aligned}
$$
(A.28)

Finally, integrating $\langle \tilde{p}(\omega)\tilde{p}^*(v)\rangle$ over ω and v gives the rms mode pressure level for the (m,n)th. The end result is

$$
\begin{aligned}
\langle p_{mn} p_{mn}^* \rangle = & \frac{1}{2\pi} \left(\tfrac{1}{2}\rho_0 N_V\right)^2 \int_{-\infty}^{\infty} \int_{r_H}^{r_T} \left\{ \frac{L_r}{\Gamma^2 k_{mn}^2(\omega)} \right\} (U_1 b)^2 |C_{mn}^2(\bar{r},\omega)| \psi_m^2(\kappa_{mn}\bar{r}) \\
& \times \left(\frac{m}{\bar{r}}\cos\alpha + \gamma_{mn}(\omega)\sin\alpha \right)^2 \{\cdots\} d\bar{r}\, d\omega,
\end{aligned}
$$
(A.29)

where $\{\cdots\}$ denotes the expression inside the curly bracket in Eq. (A.28). The per frequency contribution is therefore given by

$$\langle p_{mn}(\omega)p_{mn}^{*}(\omega)\rangle = \left(\tfrac{1}{2}\rho_0 N_V\right)^2 \left\{\frac{1}{\Gamma^2 k_{mn}^2(\omega)}\right\} \int_{r_H}^{r_T} (U_1 b)^2 L_r C_{mn}^2(\bar{r},\omega)\psi_m^2(\kappa_{mn}\bar{r})$$

$$\times\left(\frac{m}{\bar{r}}\cos\alpha + \gamma_{mn}(\omega)\sin\alpha\right)^2 \{\cdots\}\,d\bar{r}. \tag{A.30}$$

References

[1] E. Envia, Fan noise reduction: an overview, *International Journal of Aeroacoustics* 1 (2002) 43–65.
[2] S.A.L. Glegg, C. Jochault, Broadband self noise from a ducted fan, AIAA Paper 97-1612, 1997.
[3] B. Gouville, M. Roger, J.M. Cailleau, Prediction of fan broadband noise, AIAA Paper 98-2317, 1998.
[4] B.L. Morin, Broadband fan noise prediction system for gas turbine engines, AIAA Paper 99-1889, 1999.
[5] D.B. Hasson, Broadband noise of fans—with unsteady coupling theory to account rotor and stator reflection/transmission effects, NASA-CR-2001-21136, 2000.
[6] G.G. Podboy, M.J. Krupar, S.M. Helland, C.E. Hughes, Steady and unsteady flow field measurements within a NASA 22 inch fan model, AIAA Paper 2002-1033, 2002.
[7] G. Podboy, M.J. Krupar, C.E. Hughes, R.P. Woodward, Fan noise source diagnostic test—LDV measured flow field results, AIAA Paper 2002-2431, 2002.
[8] J.J. Adamczyk, M.L. Celestina, T.A. Beach, M. Barnett, Simulation of three-dimensional viscous flow within a multistage turbine, *Transactions of ASME* 112 (1990) 370–376.
[9] H. Shih, W.W. Liou, A. Shabbir, J. Zhu, Z. Yang, A new k–ε eddy viscosity model for high Reynolds number turbulent flows, *Computers and Fluids* 24 (1995) 227–238.
[10] C.S. Ventres, M.A. Teobold, W.D. Mark, Turbofan noise generation volume 1: analysis, NASA CR-16795, 1982.
[11] C.E. Hughes, Aerodynamic performance of scale-model turbofan outlet guide vanes designed for low noise, AIAA Paper 2002-0374, 2002.
[12] C.E. Hughes, R.J. Jeracki, C.J. Miller, Fan noise source diagnostic test—rotor-alone nacelle aerodynamic performance results, AIAA-Paper 2002-2426, 2002.
[13] R. Woodward, C.E. Hughes, R.J. Jeracki, C.J. Miller, Fan noise source diagnostic test—farfield acoustic results, AIAA-Paper 2002-2427, 2002.
[14] U.W. Ganz, P.D. Joppa, T.J. Patten, D.F. Scharp, Boeing 18-Inch fan rig broadband noise test, NASA/CR-1998-208704, 1998.
[15] M. Nallasamy, E. Envia, S.A. Thorp, A. Shabbir, Fan noise source diagnostic test—computation of rotor wake turbulence noise, AIAA paper 2002-2489, 2002.
[16] R. Mani, P.R. Gliebe, P.Y. Ho, Fan broadband noise model development, NASA-CR-198457, 1997.
[17] E. Envia, M. Nallasamy, Design selection and analysis of swept and leaned stator concept, *Journal of Sound and Vibration* 228 (1999) 793–836.
[18] E. Envia, Fan noise source diagnostic test—vane unsteady pressure results, AIAA Paper 2002-2430, 2002.
[19] E.J. Rice, Broadband noise radiation models for aircraft engines, Final Report for NASA Contract No. NAS3-27720, 1998.
[20] M. Nallasamy, Computation of noise radiation from fan inlet and aft ducts, *Journal of Aircraft* 34 (1997) 387–393.